AN ABSTRACT OF THE THESIS OF

Myeong Chan Jo for the degree of Master of Science in Mechanical Engineering presented on June 17, 2008.

Title: Thermally Actuated Pumping of a Single-phase Fluid using Surface Asymmetry

Abstract approved:

Vinod Narayanan

An experimental study of thermally actuated pumping of a single-phase, single-component fluid is presented in the context of thermal management of a heat source. The prominent feature of this pumping method is that the very heat that is to be removed from the heat source causes a net fluid motion. Therefore, such a thermal management system tends to be passive and noiseless. The dominant driving force for convection in this study is surface tension. An asymmetry in this force is created by the use of a surface with repeated asymmetric triangular structures.

Silicone oil was used as the working fluid. Independent parameters consisted of the channel surface-to-ambient temperature difference and the fluid thickness. A dye-tracking imaging method was developed to determine the fluid interfacial velocity. The flow results were corroborated with interfacial temperature measurements obtained using infrared thermography.

Dye tracking experiments indicate that the direction of net fluid motion is from the less-steep side of the ratchet towards its steeper side, resulting in a clockwise flow direction in the closed loop channel for all three liquid depths of 0.5 mm, 1.0

mm and 2.7 mm. The range of the net flow velocities varies from 0.18 mm/min to 0.86 mm/min. A fluid height of 1 mm results in a maximum net fluid velocity at both surface-to-ambient temperatures studied. Interfacial temperature contour maps indicate the presence of thermal structures that are indicative of convection cells, and that an optimum thickness exists for maximum heat transfer coefficient. Difference in streamwise gradients of temperature (and hence surface tension) on either side of the thermal structures causes a net streamwise surface tension gradient in the direction of net fluid motion. An optimal fluid thickness for heat transfer as well as net interfacial fluid velocity is suggested by the results.

Thermally Actuated Pumping of a Single-phase Fluid using Surface Asymmetry

by
Myeong Chan Jo

A THESIS

submitted to

Oregon State University

in partial fulfillment of
the requirements for the
degree of

Master of Science

Presented June 17, 2008
Commencement June 2009

Master of Science thesis of Myeong Chan Jo presented on June 17, 2008.

APPROVED:

Major Professor, representing Mechanical Engineering

Head of the School of Mechanical, Industrial and Manufacturing Engineering

Dean of the Graduate School

I understand that my thesis will become part of the permanent collection of Oregon State University libraries. My signature below authorizes release of my thesis to any reader upon request.

Myeong Chan Jo, Author

ACKNOWLEDGMENTS

I would like to express my sincere appreciation to my advisor, Dr. Vinod Narayanan, for his guidance, support and encouragement throughout the course of this study at Oregon State University. The motivating discussions I had with him and constant pushing from him over the years were essential in completing this work. The educational experience received from him and serious attitude toward work learned from him have undoubtedly contributed to my academic career development.

I would also like to thank my thesis committee Dr. Deborah Pence, Dr. Sourabh V. Apte and Dr. Abi T. Farsoni for their time, suggestions and comments.

My thanks also go to my wife, Ho Jin Lee, for her endless love and patience and my daughter, Se Eun (Ashley) Jo, for being able to take my mind off my work.

Special thanks also go to my parents for their faithful support and encouragement. Their unconditional support and concern helped me go through all the process.

TABLE OF CONTENTS

TABLE OF CONTENTS (Continued)

TABLE OF CONTENTS (Continued)

LIST OF FIGURES

LIST OF FIGURES (Continued)

Figure Page

LIST OF TABLES

Thermally Actuated Pumping of a Single-Phase Fluid using Surface Asymmetry

1 INTRODUCTION

The trend of high performance electronic chips is towards high power density. With this increase in dissipated heat flux, thermal management systems use single phase change liquid cooling technology have become the norm because air cooling technologies have reached their heat load limits, especially since the electronic chips must operate at a junction temperature less than 100 ºC. Liquid cooling can be implemented in a wide range of configurations, including natural convection, channel flow, jet impingement, and spray cooling [1]. However, most liquid cooling systems use mechanical pumps that result in expensive, heavy and noisy cooling systems. For this reason, many researchers have tried to design cooling systems with no or minimal power consumption, such as loop heat pipe [2-3] and capillary pumped loop [4-5]. This thesis discusses pumping of fluid using waste heat such as that generated by the electronic components. Two important factors constitute the thermally-actuated pumping. The first is the driving force for fluid flow; in this thesis Marangoni convection (surface tension) or Rayleigh-Benard convection (buoyancy) provide this driving force. The second is a geometrical factor, a surface asymmetry, which causes a spatially non-uniform force distribution that results in a net pumping effect.

The density of a liquid depends on its temperature, generally decreasing with an increase in temperature. Therefore, when a liquid layer with a free upper surface is heated from below, the warmer liquid flows upward and the cooler liquid flows downward by natural convection. This convective flow motion creates two warmer

regions due to an upwelling of warmer liquid towards the gas-liquid interface on either side of a colder region that is formed due to the descending cooler liquid (see Fig. 1.1). Since surface tension of liquid decreases with increase in temperature, the higher surface tension liquid of a colder region pulls the lower surface tension liquid of warmer regions. This motion deflects the gas-liquid interface such that the warmer regions have the thinner depths than colder regions (Fig. 1.1b). Thus, local streamwise surface tension gradients cause the local convective flow motion. This surface tension gradient is in turn established by a vertical temperature difference between the surface and ambient.

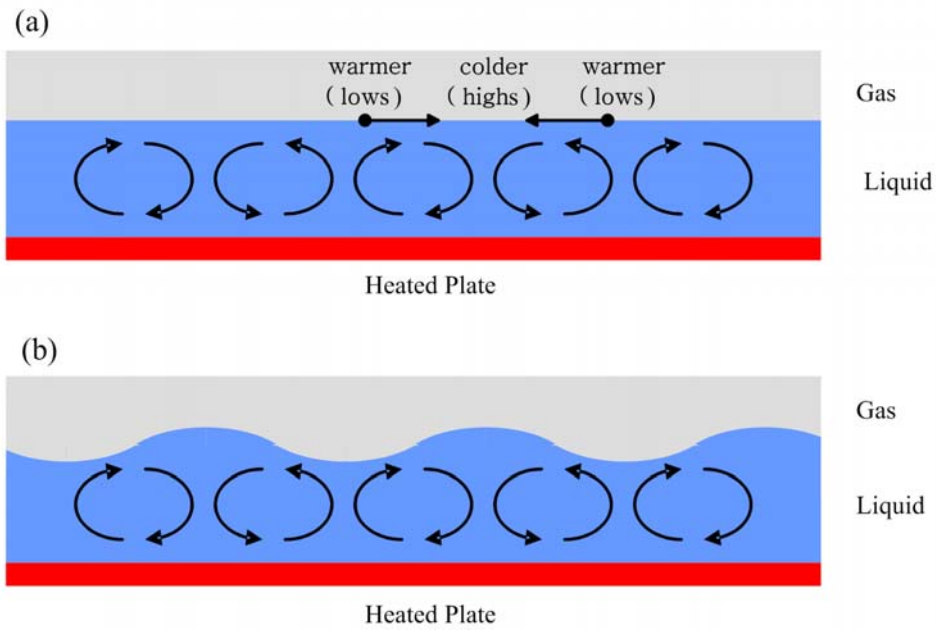

Figure 1.1 Schematic illustrating the destabilizing mechanism in Marangoni-Benard convection. (a) Fluid movement driven by surface tension gradients, (b) The resulting gas-liquid interface deflection.

The strength of surface tension forces in the system is characterized by the Marangoni number, which is the ratio of the surface tension force to the viscous force,

$$Ma = \left(\frac{d\sigma}{dT}\right)\frac{\Delta T d}{\alpha\mu} \tag{1.1}$$

where $\frac{d\sigma}{dT}$ is temperature coefficient of surface tension, ΔT is temperature difference between top surface and bottom surface of the liquid layer, *d* is thickness of the liquid layer, α is thermal diffusivity, and μ is dynamic viscosity. In this thesis, ΔT and *d* are the independent parameters that are varied in order to change the *Ma*. The strength of buoyancy forces in the system is characterized by the Rayleigh number, which the ratio of the buoyancy force to the viscous force,

$$Ra = \frac{\Delta T g \beta d^3}{\alpha\upsilon} \tag{1.2}$$

where ΔT is temperature difference between top surface and bottom surface of the liquid layer, g is gravitational acceleration, β is thermal expansion coefficient, *d* is thickness of the liquid layer, α is thermal diffusivity, and υ is kinematic viscosity. In the system, when the liquid layer is thin enough, the ratio of the Marangoni number to the Rayleigh number becomes much greater than 1. For this condition, the effect of the buoyancy forces due to gravity has a negligible contribution towards convective motion in the fluid. Therefore, surface tension gradients are dominant driving force in the convective flow. This surface tension driven flow is often referred to as Marangoni convection. On the contrary, when the liquid layer is thick enough, the ratio of the Marangoni number, *Ma* to the Rayleigh number, *Ra* is much less than 1 in the system. Under this condition, buoyancy force is the dominant driving force in the convective

flow. This buoyancy driven flow is often referred to as Rayleigh-Benard convection [6].

There are some differences between Marangoni convection and Rayleigh-Benard convection. First, Marangoni convection needs a free surface in the system that can be deformed by surface tension. However, Rayleigh-Benard convection could occur when the top surface of the liquid layer is exposed to the atmosphere as well as when the liquid is completely enclosed between rigid walls [7]. As mentioned previously, the dominant driving forces of Marangoni convection and Rayleigh-Benard convection are surface tension gradients and buoyancy force, respectively.

When the liquid has one free interface both buoyancy and surface tension gradients produce a deflection of the free surface [8]. However, they have opposite actions as shown below in Fig. 1.2. In Rayleigh-Benard convection, the warmer regions have larger liquid layer thickness than the colder regions, because the warmer liquid is rising and the colder liquid is falling by density gradients. When considering surface tension gradients on the interface, the higher surface tension liquid of colder region pulls the lower surface tension liquid of warmer region; hence warmer regions have thinner liquid layers than colder regions.

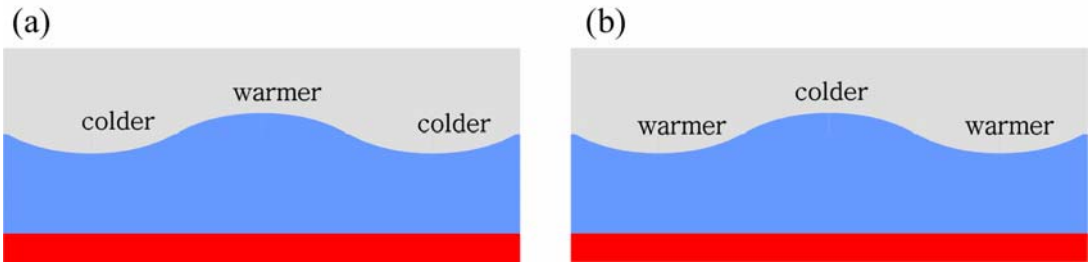

Figure 1.2 Deflection of the free surface of a liquid: (a) Buoyancy driven flow (Rayleigh-Benard convection), (b) Surface tension driven flow (Marangoni convection).

2 MOTIVATION AND OBJECTIVES

2.1 Motivation

The spatially periodic, local convective cells formed in Fig. 1.1 and 1.2 are caused by either the buoyancy or surface tension forces. Suppose an asymmetry could be introduced in this local convective cell pattern, a net movement of the fluid could potentially be realized. Linke et al [9] and Stroock et al. [10] have shown that such asymmetry in the local forces can be caused by a simple geometrical modification to the surface, such as by introduction of a periodic saw-tooth or ratcheted structures. The motivation of this study is based on the premise that thermally actuated pumping using surface tension and buoyancy forces is possible by use of surface asymmetry. In particular, this thesis identifies the potential for use of such a thermally actuated fluid motion in a thermal management scenario by examining both open loop (preliminary experiment) and closed loop (main experiment) systems.

A thermally actuated pump would use waste heat generated by the electronic component to circulate its coolant. Thus, it would eliminate the need for additional power input as well as moving parts thereby greatly reduce the weight and cost associated with thermal management technology. Thus far, few studies have investigated the effect of surface asymmetry on the Marangoni convection [10] or Rayleigh-Benard convection. Since the convection dominated by surface tension forces is expected even under zero-gravity as well as under microgravity environment, such study opens up the possibility for the application in thermal management in space systems.

2.2 Objectives

The overall goal of the present research is to experimentally identify and quantify thermally actuated pumping of a single-phase, single-component fluid, and to lay the broad foundation for identifying the feasibility of thermally actuated pumping in thermal management. The effect of the asymmetric structured surface on the Marangoni convection is documented by variation of two parameters- the liquid layer thickness as well as surface to interface temperature difference. An open channel, closed loop test section is used in which the top liquid layer is exposed to ambient air. The specific objective of this thesis is to quantify thermally actuated pumping in the closed loop system through imaging to determine flow velocity. In order to identify the thermal gradients that cause pumping, the liquid-air interface temperature is mapped spatially using infrared thermography.

The main experiment of the present study considers thin liquid layer in which surface tension is the dominant driving force; Marangoni convection. However, before the main experiment, the preliminary experiment was performed for thick liquid layers in which buoyancy is the dominant driving force. In order to quantify thermally actuated pumping due to Rayleigh-Benard convection in the preliminary experiment, the global mass flow rate induced by pumping was measured in the open loop system. Appendix A shows details of how the preliminary experiment was performed.

The present study extends Stroock et al.'s [10] study to in attempting to quantify the net velocity and streamwise temperature distributions and in exploring the relationship between the flow field and temperature distribution. The basic geometry of the asymmetric ratchets is identical to their study; however the ratchets are arranged

in a closed loop configuration (see Fig. 4.2). Also different from their study is the ratio of the height of the ratchet to the height of the liquid layers as well as the dimensions of the ratchet topology. The height of ratchets was approximately two to five times smaller in this study than the ratchets used in Stroock et al.'s [10] study. Whereas Stroock et al.'s [10] study considered several surface-to-ambient temperature differentials, the present study is limited to just two temperature differentials that are of relevance to thermal management.

3 LITERATURE REVIEW

In this chapter a review of literature concerning the Marangoni convection in a single liquid layer is presented. In addition, the most relevant previous work on the effect of surface geometry in the presence of a driving force for convective motion in a preferential direction is reviewed. Other studies exist of Marangoni convection [11, 12, 13] in two immiscible liquid layers. However, because the emphasis of this thesis is on a single liquid layer, literature in this area is not summarized.

3.1 Marangoni Convection

The Marangoni convection is now widely recognized for its practical importance, due to the fact that it is omnipresent in a large variety of processes, such as crystal growth, film coating process, and low gravity fluid experiments [6, 8]. The studies have been carried out to study the onset of convection, the pattern formation of convection, the wave number selection based on liquid thickness and so on.

Selamet et al. [14] performed a numerical analysis for Marangoni instability in a liquid layer heated from the flat bottom wall in 2-D rectangular container. The fluid was unconstrained at the top, such that a fluid-air interface existed. They assumed that Rayleigh-Benard convection due to buoyancy forces did not affect the fluid motion in their model. The effects of Marangoni number *Ma*, Biot number *Bi*, and aspect ratio on heat transfer and flow motion were investigated. In their study, the Biot number ($Bi = \frac{h_g d}{k_l}$) was defined as the ratio between convective heat transfer from the gas-liquid interface surface and heat conduction within the liquid layer. Their

numerical analysis demonstrated that the average Nusselt number increased with an increase in Marangoni number. A decrease in *Bi* caused a decrease in the average Nusselt number, because the temperature difference between the liquid-air interface and bottom wall surface decreased with decreasing Biot number. The authors also reported that the critical Marangoni number for the onset of the convection becomes smaller with increasing aspect ratio because of the increase of the number of convection cells.

VanHook et al. [15] experimentally studied Marangoni convection in very thin layers of gas (air) – liquid (silicone oil) in circular closed container. The top surface was cooled by a temperature-controlled chloroform bath. The objective of their study was to reveal a deformational instability in an initially flat liquid layer with a free upper surface. In their experiment, the thickness of liquid layer ranged between 0.005-0.025 cm and the thickness of gas layer ranged between 0.023-0.08 cm. Since the ratio of the Marangoni number to the Rayleigh number was in excess of 100 in their experimental conditions, surface tension forces were strongly dominant in the convection onset. For visualizing convection patterns, they used shadowgraph and infrared imaging. They observed the onset of long-wavelength instability due to a short wave number which was induced by the very thin thickness of liquid. The relation between the wavelength and the short wave number is the following,

$$k = \frac{2\pi d}{L}, \quad \lambda = \frac{2\pi}{k} \tag{3.1}$$

where, k is the wave number, λ is the wavelength, d is thickness of liquid layer and L is the length of the bottom plate. This long-wavelength instability produced a large scale drained region (dry spot) which had the size of one-quarter to one-third the

diameter of the circular container. The authors noted that such dry spots could be a serious problem in microgravity conditions, where fluid motion is driven mainly by surface tension gradients. They also compared their experimental results with the linear stability theory and presented their results in terms of a dynamic Bond number. The dynamic Bond number, $Bo = \frac{\rho g d^2}{(d\sigma / dT)\Delta T}$, a measure of the balance between gravity and thermocapillary forces, was identified to be the relevant control parameter for the long-wavelength instability. In the comparison with prediction of linear stability theory, the results of the experiment showed that the critical dynamic Bond number was 35% smaller than predicted value by linear theory. That is, a very thin liquid layer in the experiment could cause a premature convection onset due to the long-wavelength instability.

Ismagilov et al. [16] studied the effect of two-dimensional topographies created by triangular, hexagonal and square array patterns of pillars on Marangoni convection. Two key parameters governed the nature of the convective cells formed: (a) the ratio of the pillar to liquid height, and (b) the intrinsic wavelength of the cells in comparison with the array period and symmetry. The latter parameter could be varied by changing the liquid thickness or by changing the surface-to-ambient temperature differential. In addition to the two-dimensional post patterns, unidirectional surface topographies (linear steps) were studied. This linear step topography caused the convective cells to be constrained to the line pitch in the streamwise direction; however the structures in the spanwise direction varied with liquid height and surface-to-ambient temperature differential.

Koschmieder and Prahl [17] experimentally investigated the onset and the pattern form of Marangoni convection in small circular container. The aspect ratios (*L/d*) of container were sufficiently small such that the lateral boundaries determined the flow structure. They found that with increasing aspect ratios, the patterns with discrete rotational symmetries were observed and the number of convective cells increased. Their experiment results showed that critical Marangoni number decreased rapidly with increasing aspect ratios, corroborating findings of Selamet et al.'s [23] numerical study.

3.2 The Effect of Surface Geometry on Marangoni Convection

Literature reviewed in Sections 3.1 concerns the driving force for thermally induced convection in a single liquid layer on the heated flat bottom surface. As noted in Chapter 2, a net convective flow is obtained by creating a surface asymmetry. Literature pertaining to geometrical modifications of the bottom surface is reviewed here.

Alexeev et al. [18] studied, both experimentally and numerically, Marangoni convection of a silicone oil film of 0.5 mm thickness on a heated horizontal wall with parallel symmetrical grooves. The top surface of the oil was open to ambient air. The motivation of their study was to enhance convective heat transfer using Marangoni convection. The influence of bottom wall structures on the surface tension driven flow and heat transfer associated with convection was investigated. Flow patterns were visualized by tracking glass spheres in the liquid with CCD camera equipped by a microscopic objective. In their experiment, a cylindrical roll planform was observed in

each groove as opposed to a hexagonal planform appeared on heated flat bottom surface; see Section 3.1. The authors mentioned that these rolls are the effect of periodicity on temperature and velocity in the thin liquid films due to periodic wall shape, and the effect of the wall shape becomes small when the liquid film thickness is greatly larger (approximately 10 times) than height of wall structure. They calculated numerically average Nusselt number as a function of the liquid film thickness. The calculation results showed that not only does Marangoni convection lead to heat transfer enhancement significantly, but also an optimal film thickness which results in a maximum Nusselt number exists. They also found that heat transfer in a thin liquid layer depends on the wall shape. A sinusoidal wall shape was found to increase heat transfer rate approximately 30 percent as compared with trapezoid wall shape.

Stroock et al. [10] investigated Marangoni convection experimentally in an open top thin liquid layer on a heated horizontal structured wall. In order to comprehend the configuration effect of the heated wall on Marangoni convection pattern, symmetrically and asymmetrically structured grooves were fabricated on the surface. In their experiment, the liquid was silicone oil and thicknesses of liquid layer of 0.5 mm and 1 mm were studied. Spatial temperature variations in the oil-air interface were measured using an infrared (IR) camera, and the motion of fluid was visualized by a dye solution. They observed that Marangoni convection resulted in a net secondary flow of fluid within the test section when the thin liquid layer was heated over a surface with asymmetric grooves. This net secondary flow occurred in addition to the local convective circulation within the grooves. Their test results showed that the direction of the net secondary flow could change with thickness of the

liquid layer and the temperature difference across the liquid layer. They reported that this behavior was unexpected, because the direction of flows driven with steady pressure gradients and electric fields did not change with the magnitude of the applied fields or with the size of the system. No such net secondary flow was observed either over surfaces with no grooves or that with symmetric grooves. Their work was particularly relevant to the present study because they also conducted the effect of asymmetric surface on Maranogni convection. However, it is different from this thesis with some points. Their height and pitch size of asymmetric grooves were 5 times larger than that of the present study. In addition, they did not look at Rayleigh-Benard convection on the asymmetric surface as well as mass flow rate through open loop channel.

4 EXPERIMENTAL FACILITY & PROCEDURE

The following chapter presents the test section and experimental facility for the closed loop system. Following a description of the facility, a summary of experimental procedure is provided. More detailed experimental procedures and part drawings of the test section are in Appendix B and F, respectively. Image analysis was used to track the movement of a dye to determine the net flow velocity. Also, the interface temperature distribution was determined using IRT. In the experiment the heated-surface-to-ambient temperature difference and liquid layer thickness were the varied independent variables.

4.1 Test Fluid

Silicone oil (SIL 180, Thermo Electron Corporation) was used as the fluid for the experiments. The physical properties of the silicone oil at room temperature are listed in Table 4.1. For comparison, the properties for water are also presented in this table. Silicone oil is non-toxic and environmentally benign. Since physical properties of silicone oils are well known, they can be used to calculate the relevant parameters. Its low vapor pressure ensures reduced evaporation at the operating temperatures of this study. The temperature coefficient of surface tension for silicone oil is lower than that for water, and this is a disadvantage of using silicone oil compared with water. Fluids having a larger temperature coefficient of surface tension are generally desirable since the surface tension force is larger (see Eq. 1.1), all other physical and thermal conditions remaining identical. However, considering the lower viscosity of silicone oil compared with water, the resistance to fluid motion by viscous forces is

expected to be smaller. Also, because water evaporates readily (higher vapor pressure), it is very difficult to quantify the liquid layer thickness in the present closed loop experiments. Hence, silicone oil was chosen for the present experiments.

Table 4.1 Typical properties of SIL 180 silicone oil and water at 20ºC.

Property	**Symbol (Unit)**	**Silicone oil**	**Water**
Density	ρ (kg/m^3)	931	998
Viscosity	υ (m^2/s)	10^{-6}	5×10^{-6}
Surface tension	σ (N/m)	0.0197	0.0764
Temperature coefficient of surface tension	σ_T (N/m.K)	-6.8×10^{-5}	-1.73×10^{-4}
Coefficient of expansion	β (1/K)	0.1×10^{-3}	0.2×10^{-3}
Specific heat	C_p (kJ/kg.K)	1.51	4.18
Thermal conductivity	k (W/m.K)	0.117	0.58
Vapor pressure	p_v (mmHg)	5	17.5

4.2 Test Section

Figure 4.1 shows an assembly view schematic of the test section. It was composed of a ratcheted plate that formed the bottom wall of the channel surrounded by an insulative channel side housing heating blocks located below the ratchet plate, and an insulation casing surrounding the heating block. The major dimensions of the test section were 0.19 m x 0.071 m x 0.06 m. The ratcheted plate and the channel side housing formed the oval closed-loop, open channel. The ratchets were machined into the top surface of an oval brass plate of 5.3 mm thickness in the form of a 30°-60°-90° periodic triangular pattern. A schematic of the cross-sectional form of the ratchets with key dimensions is shown in the inset in Fig. 4.2. The ratchet height was 0.25 mm with a period of 0.58 mm. There are two ratcheted sections, each of length 101.6 mm on the front and back sides of the oval plate as shown in Fig. 4.2. The width of the open channel was 7.62 mm. The orientation of the ratchets was reversed between the front and back ends in order to complement pumping provided by each side. Thus if one were to move in a particular direction along the oval, the orientation of the ratchets would be consistent. The channel side housing was fabricated using polyvinylchloride (PVC). Viton o-rings located along the interface between the housings and the ratchet plate prevented leakage at this interface. In order to heat the fluid in the channel, two heating blocks made from carbon steel were located below the straight front and back end sections of the oval ratcheted plate. Two 3.3 mm diameter cartridge heaters, located in heating blocks, provided the necessary heat input. They were powered by a variac. Thermally conductive grease (OMEGATERM®201 Silicone paste) was applied between the ratchet plate and heating blocks to reduce contact resistance. The

sides and bottom of the heating block were insulated using PEEK™ casing. The current and voltage were observed with a set of multimeters to monitor the electrical power supplied. The calibrated Chromel-Alumel (Type-K) thermocouples were inserted at three axial locations and three vertical locations in each of the heating blocks to determine the heat flux. The top row of thermocouples was 2.54 mm from the top of the heating block. The vertical spacing between thermocouples was 7.78 mm so as to allow a for a measurable temperature difference to occur between the thermocouples, and in order to reduce uncertainty in heat flux determination. Heat flux was calculated using the thermocouples readings and the known vertical distance between thermocouples. Thermocouple data were obtained through data acquisition system (SCXI-1001, National Instruments) using a LabVIEW® program. This SCXI-1001 system has multi-channels and included built-in cold junction compensation.

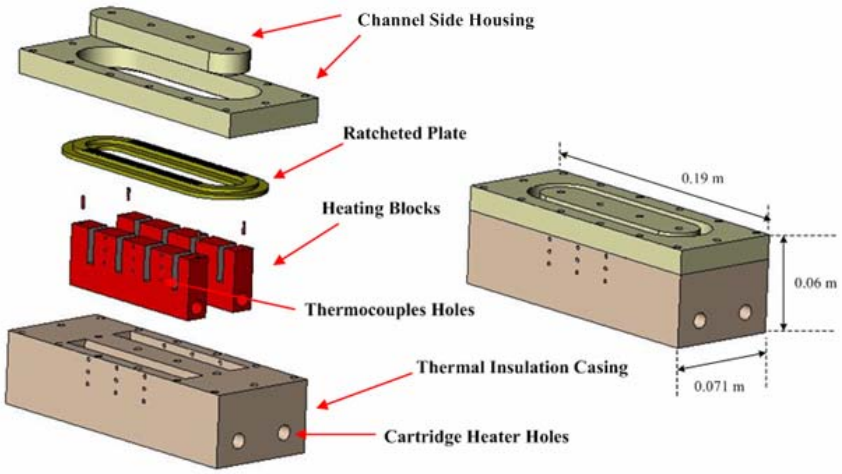

Figure 4.1 Assemble view of the experimental test section.

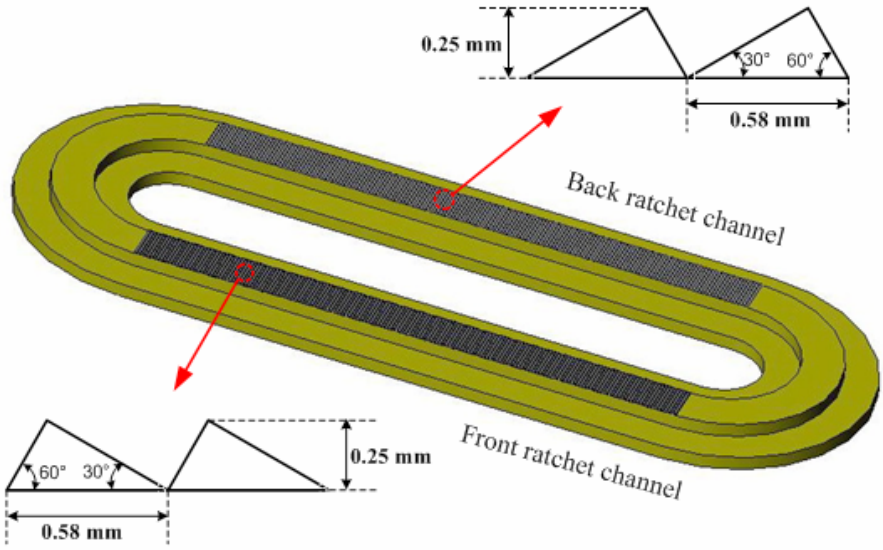

Figure 4.2 Details of the oval ratchet surface plate.

4.3 Experimental and Imaging Set-up

Figure 4.3 shows a schematic of the experimental and imaging facility. Test section was located on a precision 3-axis manual traversing system with 1 mm, 1 mm and 0.01 mm resolution in the x, y and z directions, respectively. A fairly precise vertical positioning was needed to be able to focus the oil-air interface during imaging.

The net flow induced by thermally actuated pumping of silicone oil was visualized using a CCD camera system by placing a small drop (~ 0.005 mL) of dye (Oil Blue N, Sigma-Aldrich) solution at the interface in the silicone oil. The CCD camera system consisted of a 12-bit CCD camera (Hamamatsu Photonics, Hi Sense MKII), a dedicated data acquisition processor (Dantec Dynamics Ltd., FlowMap™ System Hub), and a fiber optic illuminator (StockerYale, MILLE LUCE™ M1000). Images of the dyed region of silicone oil were captured using a Micro-Nikkor 60mm f/2.8D lens (Nikon). The FlowMap™ System Hub has a 1 GB input buffer that permitted continuous acquisition of 600 images at a resolution of 1344 x 1024 CCD pixels. Actual dimensions of the field of view imaged by the CCD camera were determined by an optical grid plate. The relation between CCD pixel and actual dimension was found by the known scale of the optical grid plate measured in CCD pixel (1 pixel = 0.0147 mm). With the pixel resolution of the camera, this calibration translates to a 19.76 mm by 15.05 mm field of view in the horizontal and vertical direction, respectively.

In order to correlate the net flow with the temperature field, radiation intensity from the oil-air interface was recorded with an Infrared (IR) imaging system. The IR imaging system (CMC Electronics, TVS 8500) with a fixed-focal-distance microscope

objective could obtain radiation intensity at 65,536 locations, corresponding to an area of 2.56 mm x 2.36 mm (256 x 236 pixels, 1 pixel = 10μm). The maximum frame rate of the imager was120 frames per second; however, this feature was not used for the present experiments.

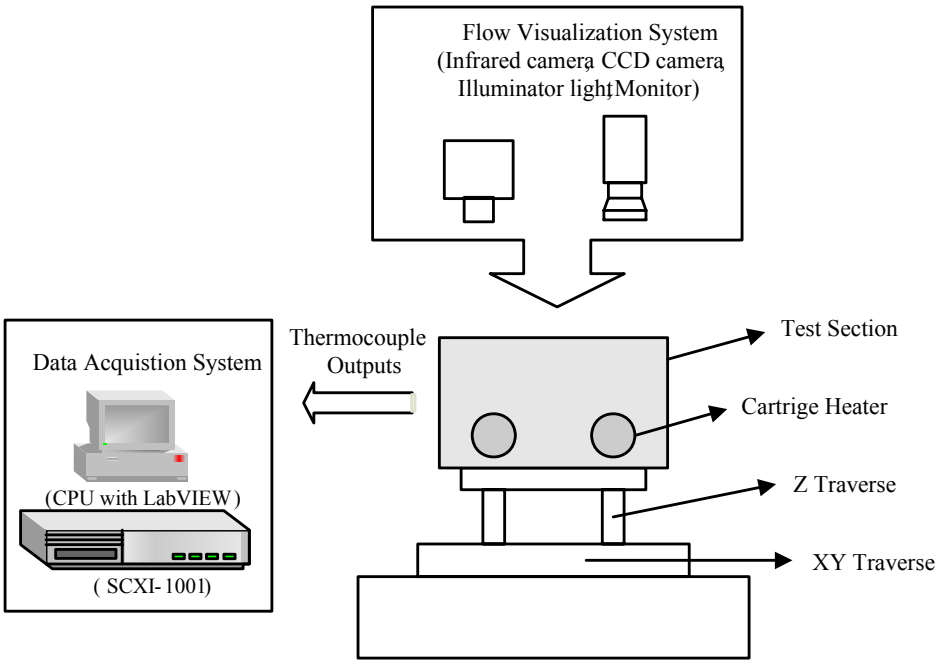

Figure 4.3 Schematic of imaging facility for the experiments.

4.4 Experimental Procedure

Table 4.2 indicates the test plan for the experiments. The surface-to-ambient temperature difference and fluid height were the varied independent parameters. Throughout this chapter, the surface-to-ambient temperature difference is presented as $\Delta T = T_s - T_\infty$, where T_s is the measured average ratchet surface temperature and T_∞ is the measured air temperature of the room. Two ratchet surface temperatures, corresponding to two surface-to-ambient temperature differentials were studied. Three fluid thicknesses, 0.5 mm, 1.0 mm, and 2.7 mm, corresponding to a *Ma/Ra* of 29.8, 7.5 and 1.0 were considered. Note that the smaller ratchet heights in the closed loop experiments permitted experimental conditions that were dominated by surface tension forces as opposed to the preliminary experiments (open loop) that were buoyancy dominated. The housing material restricted experiments at higher operating temperatures. Although it would have been interesting to observe the pumping performance at higher temperature differentials, it should be noted that *Ma/Ra* does not change with change in temperature differentials. Hence, it may be possible to distinguish between the effects of surface tension and buoyancy using these two temperature differentials.

Before starting an experiment, the ratchet plate was cleaned with a fine polishing cream, isopropyl alcohol and de-ionized water, in that order. The test section was leveled by adjusting the leveling platform. Critical to these experiments was to determine the thickness of the oil layer. Use of calipers was not ideal due to the small thickness of the oil layer and the depth of the channel walls. Hence, an alternate method was formulated to determine the thickness based on mass measurements. The

thickness of the silicone oil (d) can be related to mass from the known density (ρ), mass of added oil (m), and the area of the ratchet channel (A),

$$d = \frac{m}{\rho \cdot A} \tag{4.1}$$

The mass of silicone oil that would need to be added to the ratchet channel in order for a test fluid thickness was determined using Eq. 4.1; this mass was then measured by the digital scale (0.0001 g resolution). The measured quantity of silicone oil was poured into the oval ratchet channel. The volume of the silicone oil was calculated from the measured weight by using the known density of silicone oil at ambient temperature. Hence, the oil heights in Table 4.2 are based on a reference ambient temperature.

Critical to the success of this method of thickness determination is a precise measurement of the area of the ratchet channel. The area of the ratchet channel can be determined using the same Eq. 4.1 with area as the dependent variable. In order to permit this determination, the mass of oil corresponding to a fixed known channel depth needed to be measured. This was done by initially weighing the entire test section in the absence of silicone oil, and then adding oil till the open channel was completely full. Because the depth corresponding to the channel height was known accurately, the cross-sectional area of the channel could be determined. Appendix D documents more details on this procedure and the associated uncertainties in the oil thickness measurement. Once the oil layer was in place in the open channel, the variac that powered the two cartridge heaters was turned on. The surface temperature of ratchet plate was observed with thermocouples located 2.5 mm below the ratchet plate in the heating plates.

For CCD imaging, the dye solution was heated to the desired testing temperature to match thermal condition with the silicone oil in the channel before adding the dye solution. Then, a very small drop (~0.005mL) of the dye solution was added in the ratchet channel to track the motion of the fluid. The dyed region of the oil-air interface was recorded with CCD camera system at a rate of 1frame per second. Prior to heating the oil in the channel and addition of the dye droplet, a reference image was recorded for image processing. The net flow velocity due to a thermally-actuated pumping was determined from the CCD images by image processing using a MATLAB program presented in detail in Chapter 5.

For IRT imaging, because the IR camera records values proportional to the radiation intensity as opposed to actual temperatures, a calibration is needed to extract temperature data. Since the conversion factor for intensity to temperature is a function of temperature a calibration experiment in which spatial intensity variations at fixed, known temperatures is needed. Ideally, an in-situ calibration at each height and temperature would be required for this experiment since intensity variations could potentially occur with thickness of the oil layer at a particular temperature depending on the opacity of silicone oil (which was unknown). At each known interface temperature, a well-stirred liquid would be needed during calibration in order to prevent formation of convection cells. Also the well-stirred liquid would permit using the measured thermocouple temperatures below the oval ratchet plate as the known calibration temperatures (accounting for minor conduction resistances). However, stirring the liquid in the open channel was not an option since it would deform the oil-

air interface whose intensity is to be recorded. Stirring is also especially difficult for thin liquid layers.

Because of the challenges associated with a detailed in-situ calibration mentioned above, a simpler, albeit less accurate, calibration scheme was adopted for the present experiments. The calibration equation was generated using a separate set of experiments. From preliminary experiments, it was observed that the dimensions of the convective cells formed for larger oil thicknesses were about 4 times that of the field of view of the IR camera and that the intensity distribution within the field of view of the camera was fairly uniform within a convective cell. Hence, for calibration, IR images were recorded at the oil-air interface with a channel height of 8 mm. These images were recorded at 9 different ratchet temperatures as measured by the near-surface thermocouples. Because there was no reasonable way to extrapolate the near-surface thermocouple temperatures to the oil-air interface, these thermocouple data were used in the generation of calibration curve. The difference in location between the reference thermocouple temperatures and the temperature of the oil-air interface would then be accounted for as a bias error in the uncertainty analysis, as shown by Krebs [19]. The calibration curve is shown below in Figure 4.4.

Once the calibration curve was obtained, intensity maps were recorded at a specific location at the back side of the oval channel as per the test matrix in Table 4.2. Once the surface temperature of the ratchet plate reached steady state at the desired temperature, five intensity images of the oil-air interface were recorded with infrared (IR) imaging system. These intensity values of the image were then converted to the temperature values using the calibration equation.

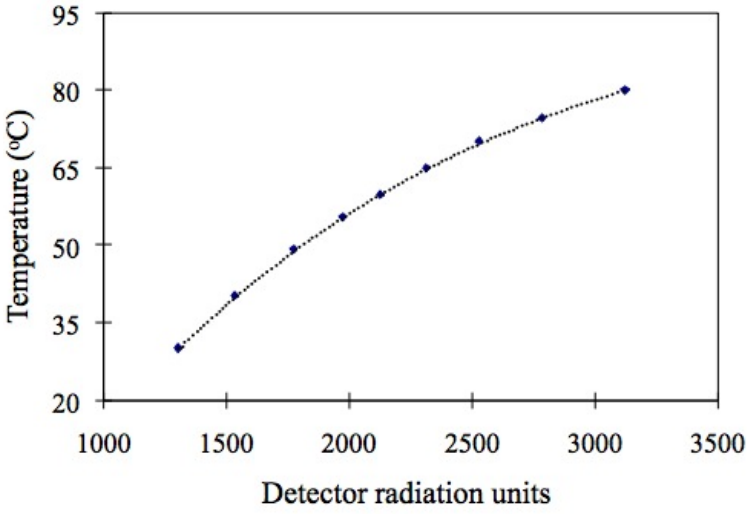

Figure 4.4 Intensity to temperature calibration curve.

Table 4.2 Summary of test plan used for data collection in the experiments.

Average ratchet surface temperature (° C)	**Oil layer thickness (mm)**	**Ratio oil thickness to ratchet height**	***Ma***	***Ra***	***Ma/Ra***	**Dominant driving force (Buoyancy / Surface tension)**
60	0.5	2	15,302	513	29.8	Surface tension
	1.0	4	30,603	4,106	7.5	Surface tension
	2.7	10.8	80,820	82,628	1.0	Comparable
80	0.5	2	22,952	770	29.8	Surface tension
	1.0	4	45,905	6,160	7.5	Surface tension
	2.7	10.8	121,231	123,942	1.0	Comparable

5 DATA REDUCTION AND ANALYSIS

In this chapter, data reduction methods for the determining net flow velocity and interfacial temperature is presented. A brief overview of the associated uncertainty analysis in these data presented. A detailed uncertainty analysis is provided in Appendix D.

5.1 Net Flow Velocity

The average velocities of moving dyed regions induced by thermally actuated pumping were obtained by tracking the center of mass of each image corresponding to the elapsed time after the addition of the dye solution. Since the dye diffused with time in silicone oil forming irregular interface shapes, it was hard to trace the movement of the dyed region of silicone oil from the raw images recorded by CCD camera. Figure 5.1 is a typical recorded image after 5 seconds of addition of the dye droplet to the oil-air interface. Note that reflection of surrounding light from the brass surface caused corresponding high intensity regions making it difficult to track the dyed region. Therefore, the raw images were enhanced through image processing in a MATLAB® program.

Prior to heating the oil in the channel and addition of the dye droplet, a reference image such as that in Fig. 5.2, was obtained. Subtraction of the pixel intensities between the dye image (Fig. 5.1) and the reference image (Fig. 5.2) allowed for the removal of the high intensity ratchet regions. The resulting image, shown in Fig. 5.3, indicates that the high intensity regions are significantly diminished. However, the difference in intensity between the dyed region and the non-dyed region

is not very large in this image. Hence, the image in Fig. 5.3 was binarized based on a user-defined input threshold using ‘im2bw’ function of the image processing toolbox in MATLAB® (see Fig. 5.4). The function converts the input image to grayscale format first, and then uses thresholding to convert the grayscale image to binary. The output binary image has values of 1 (white) with luminance greater than specific level and 0 (black) in the input image as shown in Fig. 5.4. Because there is noise due to binarization of the ratcheted surface, a 2D median filtering function, ‘medfilt2’, was applied to reduce the surface noise. The value of an output pixel is determined by the median of the neighborhood pixels rather than the mean. Since the median is much less sensitive than the mean to extreme values (outliers), the median filtering can remove the outliers without reducing the sharpness of the image. The resulting image, shown in Fig. 5.5, has little to no noise from the ratcheted surface.

With the dye region clearly defined, the next step aims to determine the center of mass of the region and track this in order to determine the dye movement from one frame to the next. The binary intensity of the image in Fig. 5.5 was inverted such that nonzero pixels belong to the dyed region and 0 pixels comprised the background. The boundary of the dyed region in the image was traced by ‘bwtraceboundary’ function of the image processing toolbox in MATLAB (see Fig. 5.6). Before tracing the boundary, specific row and column coordinates of a pixel on the border of the dyed region were defined by the user as the starting point for tracing the boundary. After tracing the boundary of the dyed region in the image, the center of mass within the dyed region was determined (red cross point of Fig. 5.6).

Once the center of mass of the dyed region was found for each image, the displacements of the center of mass between each one-minute-interval image pair was used to determine a velocity of the fluid due to thermally-actuated pumping. It was found that displacement rate (velocity) was not identical between each of the 10 one-minute-interval image pairs. Hence, an average velocity was determined over a 10-minute interval by averaging 10 velocities.

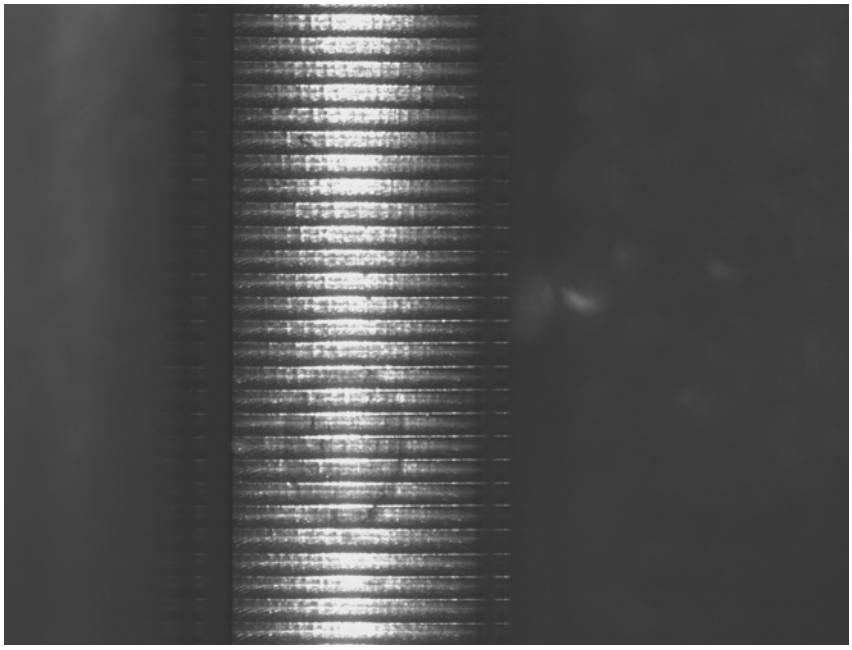

Figure 5.1 Raw image without image processing.

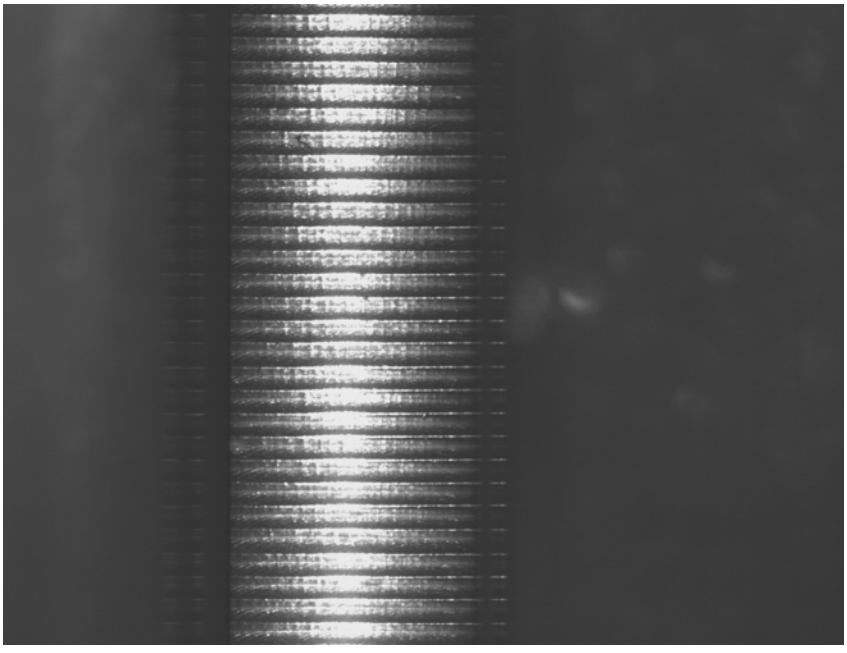

Figure 5.2 Reference image for image subtraction recorded.

Figure 5.3 Image after subtracting the reference image from the raw image.

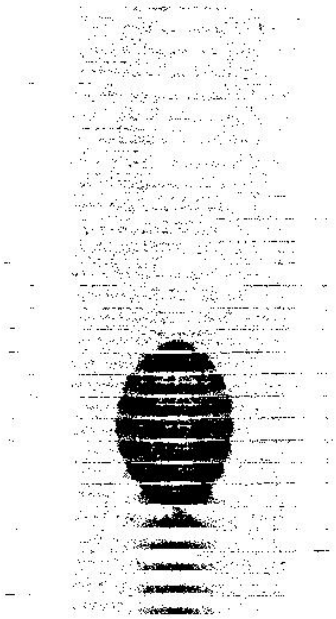

Figure 5.4 Binarized image of dye

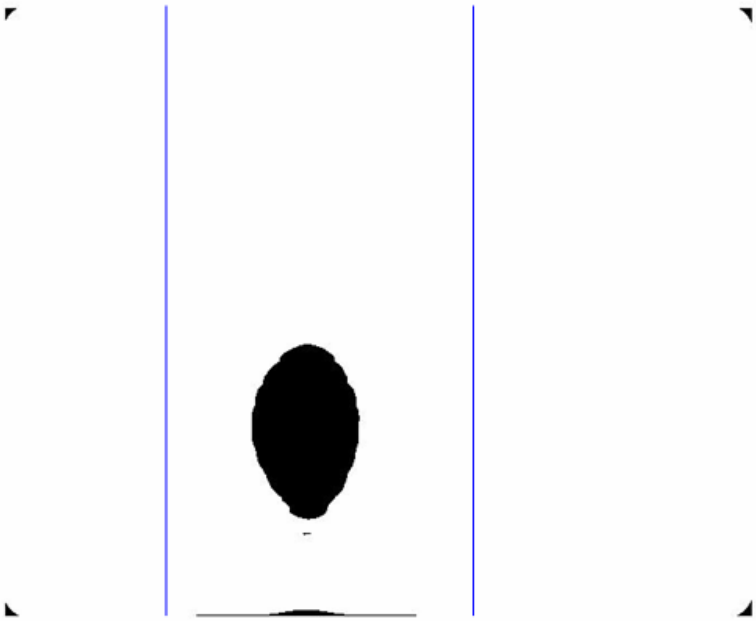

Figure 5.5 Median filtered image of dye.

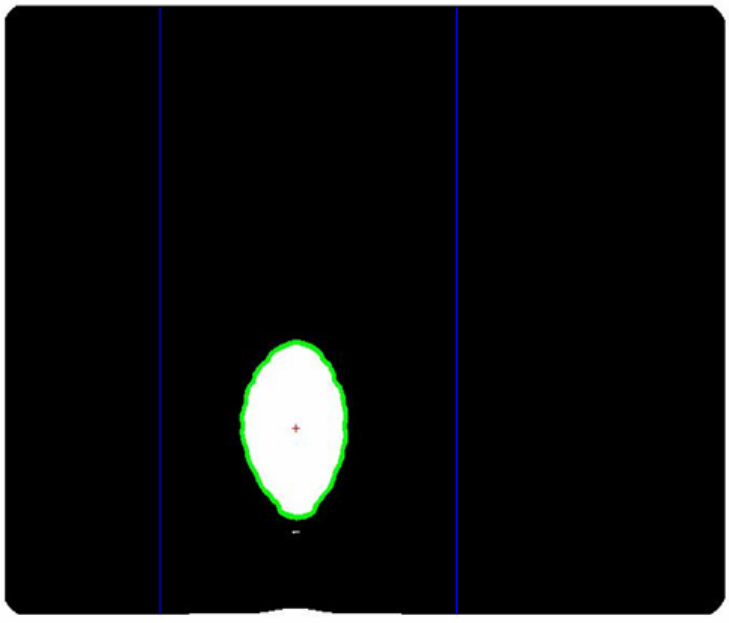

Figure 5.6 Tracing the boundary of the dyed region & determining the center of mass.

5.2 Temperature Distribution

In the present study, infrared thermography used to perform detailed temperature distribution at the oil-air interface in the channel. Since infrared thermography measures radiation intensity values of object, not temperature, the intensity values obtained should be calibrated with temperature. The calibration procedure was mentioned in detail in Chapter 4.

The calibration curve that is obtained between the intensity values of IR images and three reference temperature measured by the calibrated thermocouples is shown in Fig 4.4 for a single pixel. Each of the 65,536 pixels has a similar calibration curve. The intensity at each pixel in an experimental intensity image is converted to temperature using pixel-specific calibration curve. A typical intensity image and the converted temperature image for an experimental condition are shown in Fig. 5.7 and 5.8.

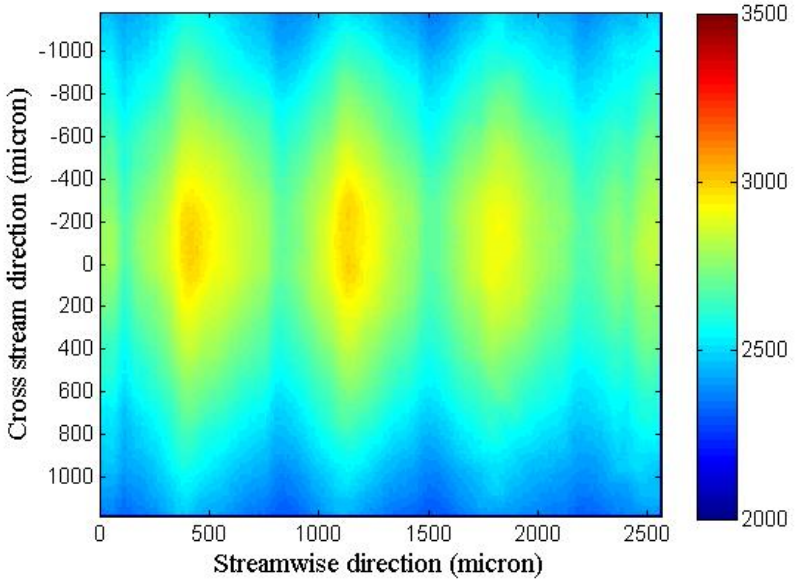

Figure 5.7 Intensity image for 0.5 mm thickness and 80 ºC ratchet surface temperature.

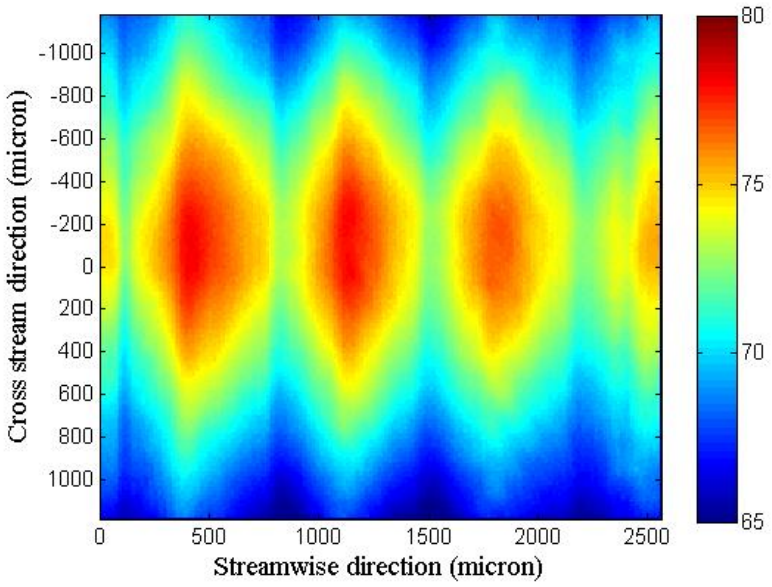

Figure 5.8 Converted temperature image for 0.5 mm thickness and 80 ºC ratchet surface temperature.

5.3 Uncertainty Analysis

5.3.1 Thickness of silicone oil

Uncertainty in the thickness of the silicone oil was determined by applying the Kline-McClintock method to Eq. 4.1. A typical uncertainty value in material property of ± 2 % for density of silicone oil was applied. Uncertainty in the mass of silicone oil consisted of bias error associated with resolution of mass balance and precision error for mass measurement. Uncertainty in area consisted of uncertainty in density of silicone oil, uncertainty in channel height and uncertainty in mass of added fully the silicon oil. Appendix D shows details of how these uncertainties were determined. Uncertainty value in thickness of silicone oil is reported in Table 5.3.

Table 5.1 Uncertainty in thickness of silicone oil in closed loop system for 1 mm.

m (g)	ρ (kg/m^3)	A (mm^2)	u_m (g)	u_ρ (kg/m^3)	u_A (mm^2)	u_d (mm)	%
2.262	931	1667	0.001	18.62	93.96	0.09	9.1

5.3.2 Temperature and Heat Flux

Heat flux supplied by cartridge heaters was calculated based on the calibrated thermocouples readings and the known vertical distance between thermocouples.

$$q'' = k\frac{\Delta T}{\Delta x} \tag{5.1}$$

Heat flux for the closed loop system was determined using Eq. 5.1. Uncertainty in the heat flux was determined by applying the Kline-McClintock method to Eq. 5.1. Appendix D shows details of how this uncertainty was determined. Uncertainty in the heat flux consisted of uncertainty in property of material, uncertainty in temperature measurement, and uncertainty in the vertical distance measurement between thermocouples. The thermal conductivity of the heating block (1018 carbon steel) is k = 51.9 W/m-K; a typical uncertainty value in material property of ± 2 % for thermal conductivity of heating block was applied. Uncertainty in temperature measurement consisted of bias error associated with the calibration of thermocouples and precision error due to fluctuation of temperature during the experiment. Uncertainty values in heat flux for 60 °C and 80 °C case of ratchet surface temperature are reported in Table 5.2.

Table 5.2 Uncertainty in temperature and heat flux.

Average ratchet surface temperature	u_T (°C)	$u_{\Delta T}$ (°C)	$u_{\Delta x}$ (mm)	u_k (W/m-K)	$u_{heat\ flux}$ (W/m^2)	%
60 °C	0.02	0.05	0.016	1.04	166.34	6.96
80 °C	0.02	0.03	0.016	1.04	179.35	5.03

5.3.3 Net Flow Velocity

Uncertainty in the net flow velocity induced by thermally actuated pumping was dependent upon the uncertainty in the displacement of the center of mass of the dyed region determined by image processing and the uncertainty in time. Since uncertainty in camera timing is given by the manufacturer to be 33×10^{-9} s, it was neglected in uncertainty calculation of the net flow velocity. Uncertainty in displacement was largely dependent upon uncertainty in the image processing. Three uncertainty parameters were included in the image processing, that is, uncertainty in subtraction, binary converting, and median filtering. Uncertainty in the image processing was determined by applying the sequential perturbation method. Uncertainty values in the net flow velocity for all cases are reported in Table 5.3. Appendix D shows details of how this uncertainty was determined.

Table 5.3 Uncertainty in net flow velocity.

Cases	0.5mm 60 °C	0.5mm 80 °C	1mm 60 °C	1mm 80 °C	2.7mm 60 °C	2.7mm 80 °C
$u_{\Delta x}$ (mm)	0.499	0.379	0.507	0.491	0.382	0.385
$u_{\Delta t}$ (min)	5.5E-10	5.5E-10	5.5E-10	5.5E-10	5.5E-10	5.5E-10
$u_{velocity}$ (mm/min)	0.050	0.038	0.051	0.049	0.038	0.038
%	14.39	8.06	9.56	5.68	10.96	5.38

5.3.4 Temperature Distribution

Uncertainty in temperature distribution obtained using IR system consisted of bias error associated with the calibration of the thermocouples used in calibration of the IRT images, precision error which is a standard deviation of temperature data obtained from IR images using calibration equation, and the calibration curve fit error of IR image. Note that the bias error during calibration due to location mismatch between the near-surface thermocouples and the oil-air interface is not included in this estimate since it cannot be estimated. Uncertainty value in temperature determined using IR system is reported in Table 5.4. Appendix D shows details of how these uncertainties were determined.

Table 5.4 Uncertainty in temperature obtained using IR.

Average ratchet surface temperature	Bias error (°C)	Precision error (°C)	Calibration curve fit error (°C)	u_T (°C)	%
60 °C	0.338	0.262	0.53	0.68	1.13
80 °C	0.338	0.199	0.53	0.66	0.83

6 RESULTS AND DISCUSSION

Experiments in the closed loop facilities were gathered according to the test plan and procedures outlined in Chapter 4, and analyzed using the methods outlined in Chapter 5. In this chapter, net flow velocity and temperature distribution induced by thermally actuated pumping are presented and discussed. As mentioned previously, two independent parameters: the surface-to-ambient temperature differential and the fluid thickness, were varied in the experiments to cause a variation in the Marangoni and Rayleigh numbers.

6.1 Net Flow Velocity

A very small droplet (~ 0.005 mL) of the dye solution was added to the oil in the closed-loop open channel to trace the movement of the fluid. The raw images were enhanced through image processing with MATLAB program to determine the displacement of the dyed region, as discussed in Chapter 5. In order to confirm the consistency of the direction of the net flow, the images of both ratchet sides (front and back, see Fig. 6.1) were analyzed for all experimental conditions summarized in Table 4.2. As a result of experimentation, the direction of the flow was negative for all experimental conditions. The arrows indicate the direction of the net flow in the Fig. 6.1. This direction of net fluid motion is different from the results of the preliminary experiments in the open loop system. Note that the thicknesses of oil layer were different (smaller) compared with the open loop system, resulting in smaller *Ma* and *Ra* numbers and larger *Ma/Ra*.

Figure 6.2 shows images of the position and pattern of dyed regions for the back ratchet channel with progression in time. Figure 6.3 illustrates a similar progression of images for the front ratchet channel. The elapsed time after adding the solution dye in the silicone oil is shown accompanying each image. Since trends of progression are similar for all silicone oil thicknesses and ratchet surface temperatures, only images for the case of 1 mm silicone oil thickness and temperature difference of 57.5 °C are presented. The average air temperature of the room during experiment was 22.5 °C. In the Fig. 6.2, the black region corresponding to the dye droplet for the back ratchet channel moves to the left side of the channel with the lapse of time. On the other hand, the black spot of the dyed region for the front ratchet channel moves to the right side of the channel as the Figure 6.3. Therefore, the direction of the net flow produced by thermally actuated pumping is consistent.

Figures 6.4 to 6.6 show the results of tracking the displacement of the center of mass (COM) in the dyed regions for the cases of the 0.5 mm, 1.0 mm, and 2.7 mm oil thickness, respectively for a temperature difference of 57.5 °C. The slopes in graph would indicate the fluid velocity. The displacement rates as a function of time were not perfectly linear partly due to the variations in ratchet geometry during fabrication and due to some variations in the ratchet surface temperature along the channel. The velocities calculated at the t = 10 minute are prone to errors since the dye droplet is not completely in view and the center of mass will be skewed towards the field of view; thereby indicating a reduced velocity. If the dyed region was partially in view, the largest dyed region was used for calculation of velocity. For the case of 1 mm silicone oil thickness, the dyed region moved farthest than other cases and the

displacement of the 0.5 mm layer case was smallest, indicating an optimum thickness among the 3 cases tested.

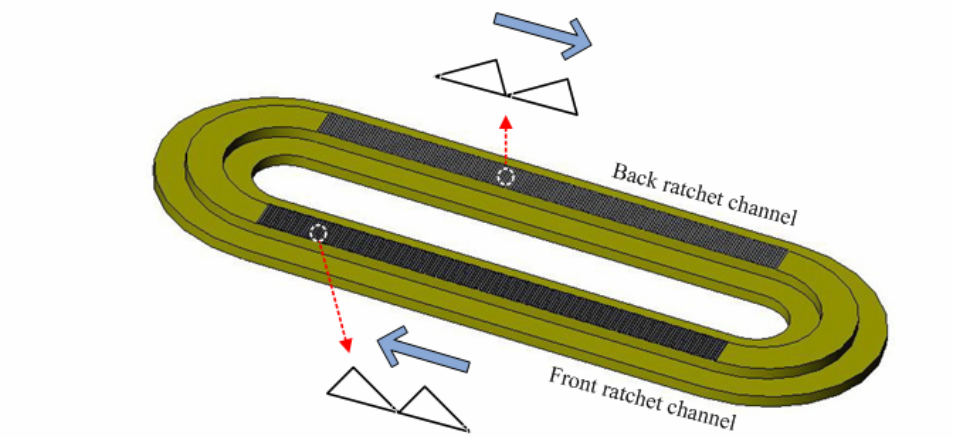

Figure 6.1 The direction of the net flow induced by thermally actuated pumping.

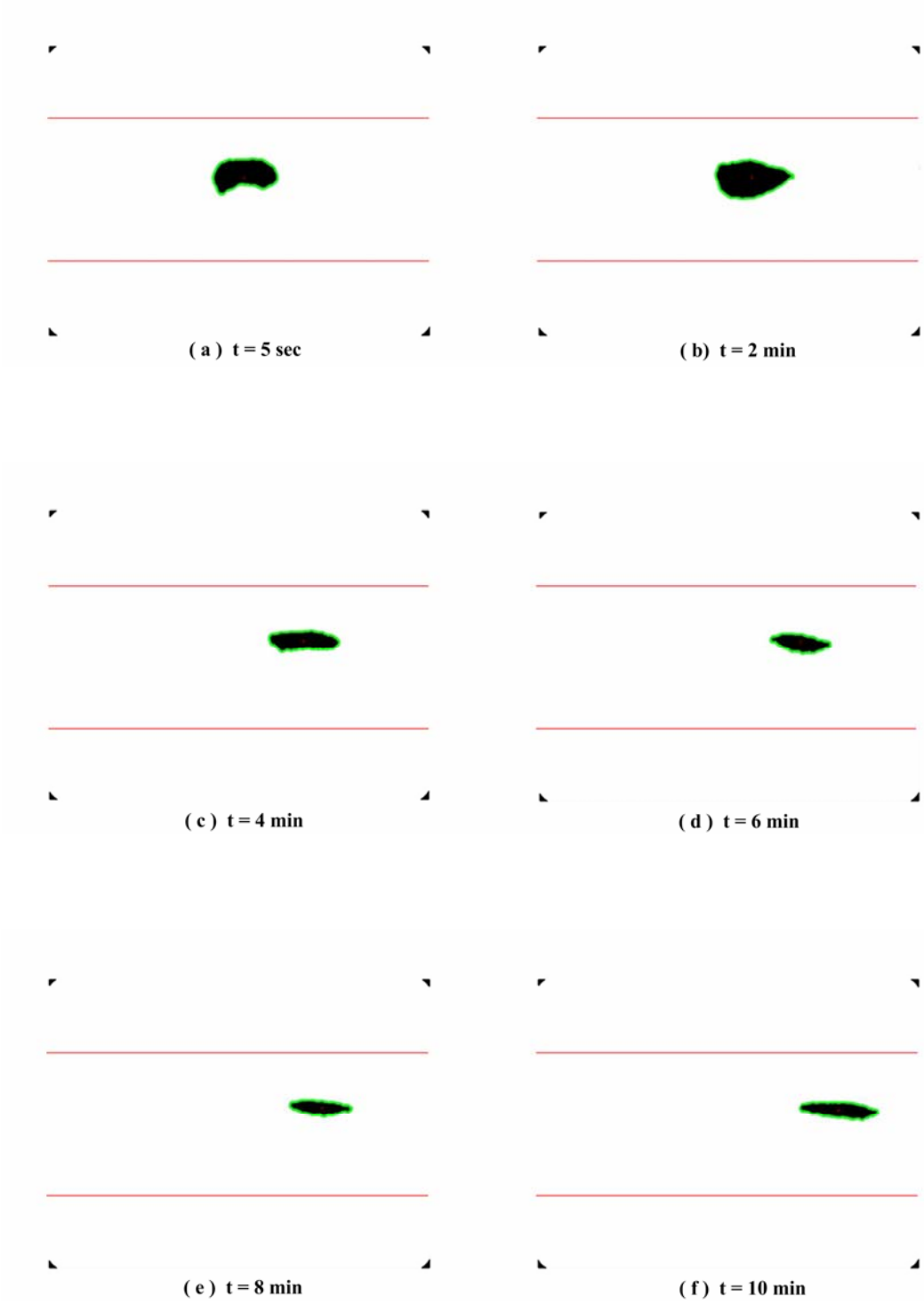

Figure 6.2 The images of the progression of the position and pattern of dyed regions for the back ratchet channel for $\Delta T = 57.5$ °C; d = 1 mm.

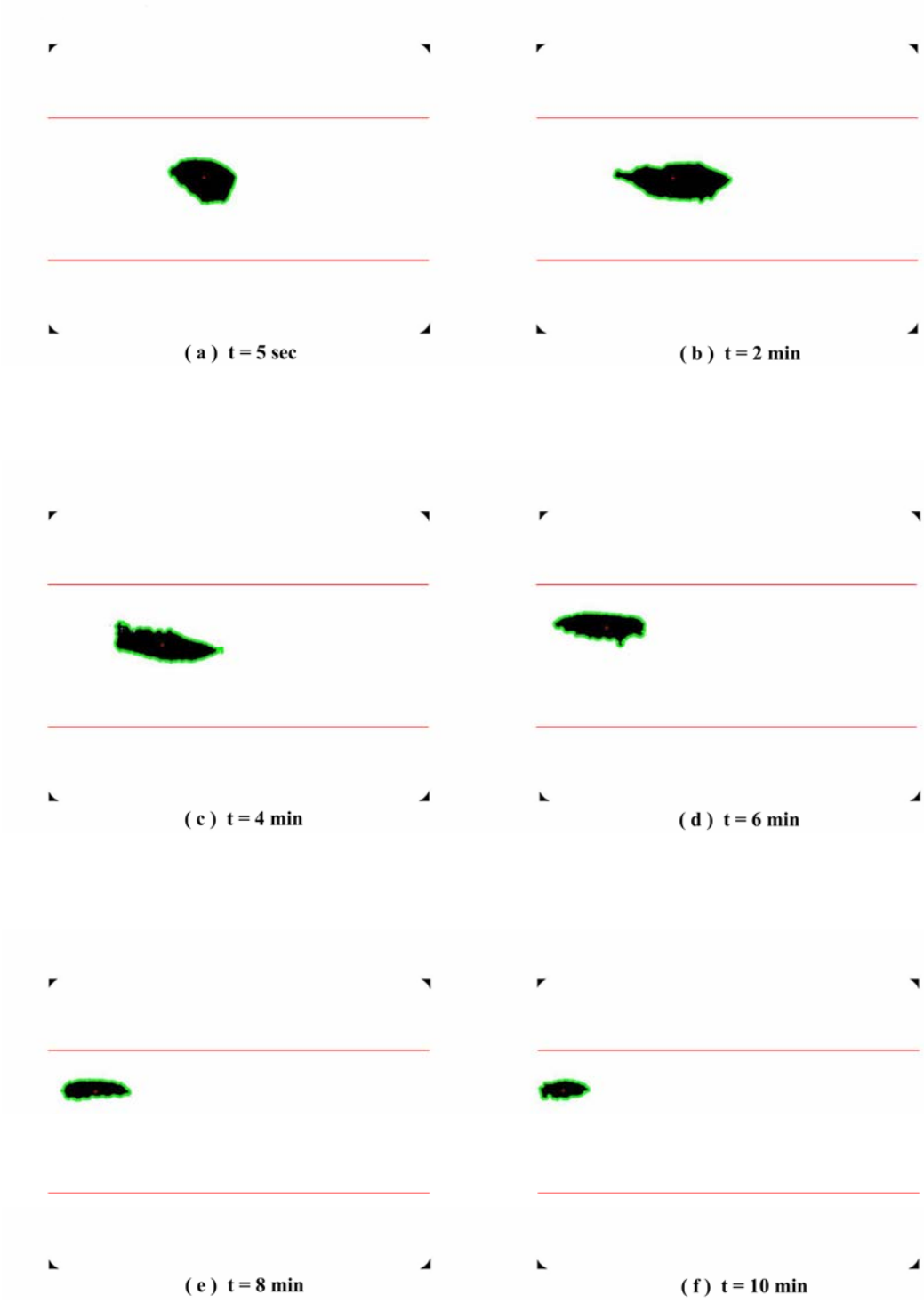

Figure 6.3 The images of the progression of the position and pattern of dyed regions for the front ratchet channel for $\Delta T = 57.5$ °C; d = 1 mm.

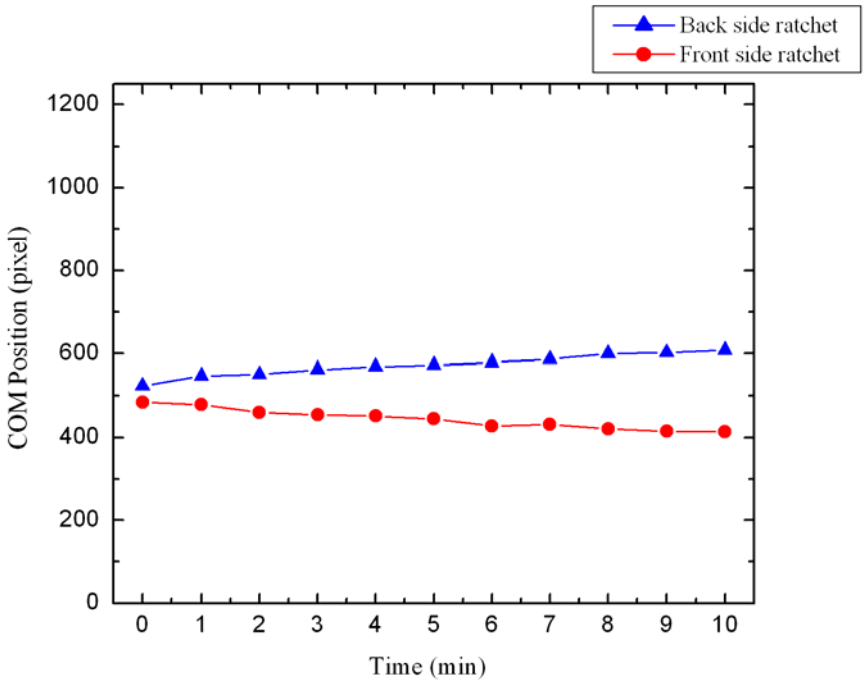

Figure 6.4 Displacement of the center of mass (COM) position of the dyed region for the silicone oil thickness of 0.5 mm; $\Delta T = 57.5$ °C.

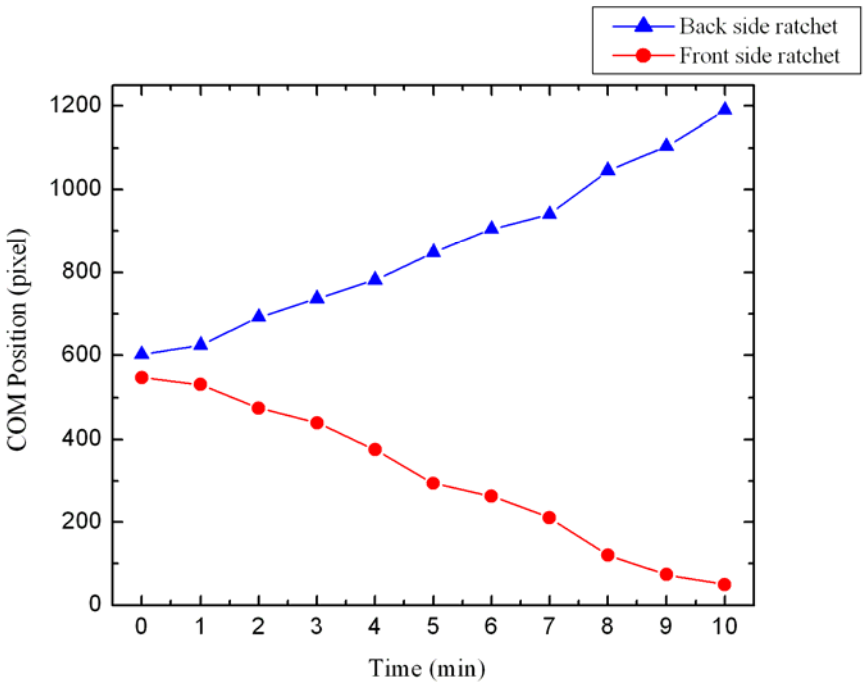

Figure 6.5 Displacement of the center of mass (COM) position of the dyed region for the silicone oil thickness of 1 mm; $\Delta T = 57.5$ °C.

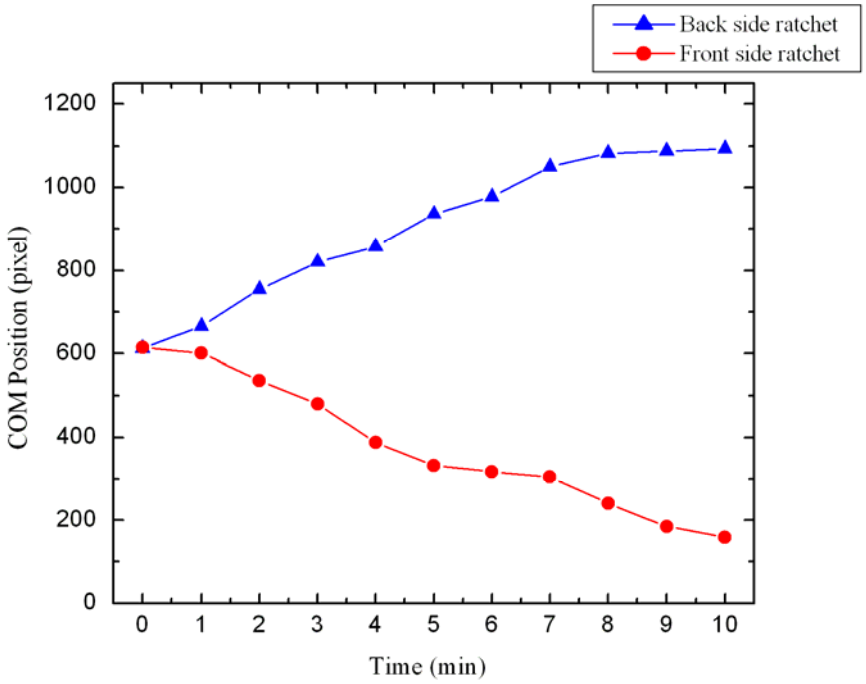

Figure 6.6 Displacement of the center of mass (COM) position of the dyed region for the silicone oil thickness of 2.75 mm; $\Delta T = 57.5$ °C.

Figure 6.7 presents the average net flow velocity as a function of three different thicknesses of the silicone oil layer for two temperature differences of 37.5 ^{o}C and 57.5 ^{o}C. Average heat fluxes of 2,626 W/m^2 and 4,013 W/m^2 were applied to the ratcheted plate for the temperatures difference of 37.5 °C and 57.5 ºC, respectively. In the present study, the ratios of the Marangoni number to the Rayleigh number for 0.5 mm, 1.0 mm, and 2.7 mm are 29.8, 7.5, and 1.0, respectively. Therefore, surface tension forces are dominant in fluid convection in the 0.5 mm and 1.0 mm fluid thickness experiments. On the other hand, both surface tension force and buoyancy force are comparable for the 2.7 mm case. A peak interfacial net velocity of ~ 0.85 mm/min was observed for the 1 mm oil thickness and 57.5 ^{o}C temperature difference

experimental condition. The net flow velocity was larger for $\Delta T = 57.5\ ^{o}C$ compared with $\Delta T = 37.5\ ^{o}C$, consistent with the larger surface tension driving force at larger temperature differentials (see Eq. 1.1).

Marangoni number, which is the ratio of the driving force provided by surface tension to the retarding viscous force, increases with increase in liquid thickness for a fixed temperature differential. Hence it would be expected that the net flow velocity be larger with increasing liquid thickness. However, the buoyancy effects also begin to gain importance at larger thicknesses (see Table 4.2). At 2.7 mm thickness case, both Marangoni and buoyancy effects are comparable and the reduction in velocity at larger thickness could be in part due to the competition in the flow direction between surface tension and buoyancy. It should be noted that the deflection of the interface is contrary for buoyancy driven flows compared with convection driven by surface tension. Perhaps a more important factor for the reduction in velocity from 1 mm thickness to 2.7 mm is the ratio of the liquid height to the ratcheted structures. For large liquid to ratchet height ratios, the ability of the ratchets to modulate the intrinsic convection cells is diminished and hence, the net flow is lower. The trend in the interfacial velocities becomes clearer in light of the interface temperature distribution results presented in the next section.

Prior studies [16, 18] have noted that the ratio of the ratchet height to the liquid layer height was an important parameter in determining the shape and size of the primary circulation pattern. Recall that these studies examined the effect of symmetric surface structures on Marangoni convection. Alexeev et al [18] found that an optimum thickness existed for which Nu was a maximum. At such a thickness, they

hypothesized that the effect of Marangoni convection was most dominant. For an asymmetric ratchet topology, Stroock et al. [10] hypothesized, based on infrared images of the interface, that the period of convection cells increased with increase in liquid-to-ratchet height ratio. Convection cells that matched the period of the ratchet were hypothesized for liquid heights that were half the ratchet period. For such conditions, the net direction of pumping changed at a temperature difference of ~ 90 ^{o}C. For liquid heights that were equal to a period of the ratchet, they found that the net pumping direction was from the 30-degree slope towards the 60-degree slope of the ratchet and that this direction remained unchanged with an increase in temperature difference. In the present experiments, even the smallest liquid layer thickness of 0.5 mm corresponded to an approximately period doubled situation as described by Stroock et al. [10]. The direction of net flow agrees well with Stroock et al. [10]'s results for the same oil thickness (1 mm) and surface-to-ambient temperature difference. However, magnitude of the net flow velocities is much larger in the present study. Stroock et al.'s [10] estimated the interfacial velocity to be 0.06 mm/min for d = 1 mm and T = 60 °C. Whereas the liquid height was similar between the two studies, liquid thickness to the ratchet period was approximately 1.7 compared with Stroock et al.'s [10] experimental condition in which ratio of the liquid thickness to the ratchet period was closer to unity.

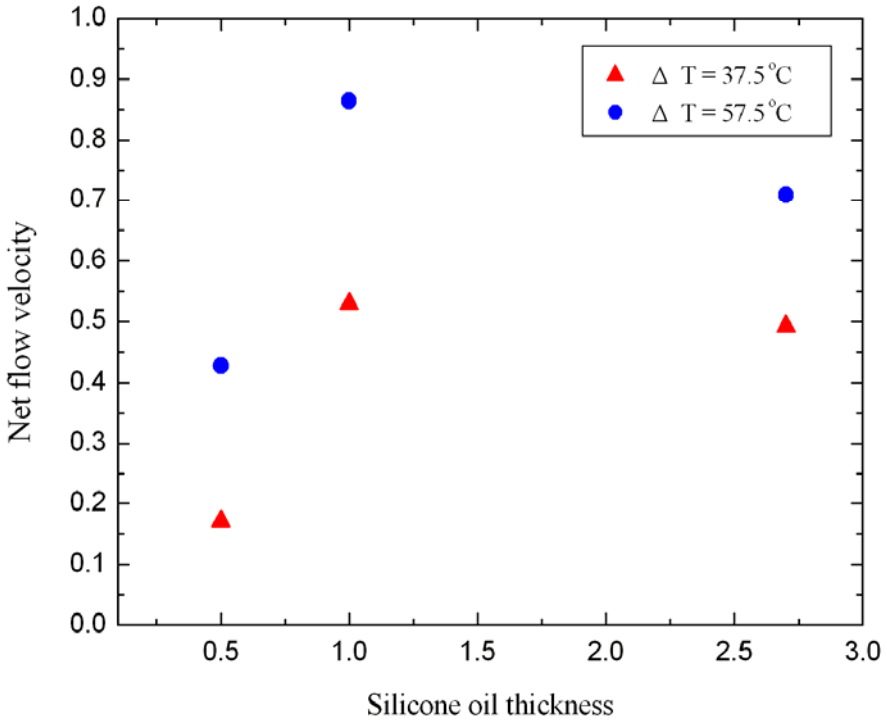

Figure 6.7 Net flow velocity as a function of temperature difference and heat flux.

6.2 Temperature Distribution

Figures 6.8 (a)–(c) and 6.9 (a)-(c) show the spatial temperature field at the oil-air interface obtained by infrared thermography for the liquid thicknesses of 0.5 mm, 1.0 mm and 2.7 mm and temperature difference of 37.5°C and 57.5°C respectively. Shown in solid black lines are the troughs of the ratchet. The crests of the ratchet are indicated as dotted lines. The location of the ratchet crests and troughs are slightly different from (a) to (b) due to movement of the test section upon cleaning and realignment following each experiment.

Thermal maps for both 0.5 mm and 1.0 mm liquid thicknesses show the same basic features of streamwise variation in temperature due to the non-uniform streamwise liquid depth caused by the structured surface. The peak interfacial temperature occurs within 0.1 mm of the crest of the ratchet for both liquid thicknesses. These high temperature regions represent upwelling of hot fluid from the surface. The thermal structures are representative of the convection patterns due to Marangoni convection. One prominent difference between the 1.0 mm and 0.5 mm thicknesses is that a much larger portion of the interfacial area is at higher temperature. Because the surface temperature and heat flux are identical for the two liquid heights, a higher surface temperature is an indication that the heat transfer coefficient is larger for the 1 mm thickness.

The temperature contours of the 2.7 mm (Figs. 6.8 (c) & 6.9 (c)) indicate that the heat transfer coefficient is lower for this thickness compared with the 1 mm thickness. As mentioned before, for Marangoni convection over symmetric grooves, Alexeev et al. [18] determined that there was an optimal liquid thickness for which the

Nusselt number was a maximum. The present study shows that such a trend seems to hold good for asymmetric geometries as well. For asymmetric geometries, it is hypothesized based on the flow and heat transfer results presented here, that not only is the heat transfer enhanced due to Marangoni convection at some optimal liquid thickness, but the interfacial velocity also reaches a maximum at this thickness.

The size of the convective cells can be gleaned from the interfacial thermal structures. The size of the thermal structures are constrained to the period of the ratchet (0.58 mm) for both 0.5 mm and 1 mm thicknesses. Alexeev et al. [18] observed that Marangoni convection cells were constrained within a period of the symmetric groove. In their IR visualization, Stroock et al. [10] observed high intensities in the streamwise direction that were ratchet-period doubled for liquid thicknesses that were approximately equal to the ratchet period. For an experimental condition that was closest to that of Stroock et al. [10] (0.5 mm thickness; ~ 0.86 ratchet period), no period doubling of the thermal structures was observed (see Figs. 6.8 (a) & 6.9 (a)). Furthermore, the period of the thermal structures did not change with a doubling of the liquid thickness to 1 mm (~1.7 ratchet periods). For a liquid thickness of 2.7 mm (~ 4.7 ratchet periods), the period of the thermal structures was larger than the field of view of the camera which was 2.5 mm or 4.4 ratchet periods; see Figs. 6.8 (c) & 6.9 (c).

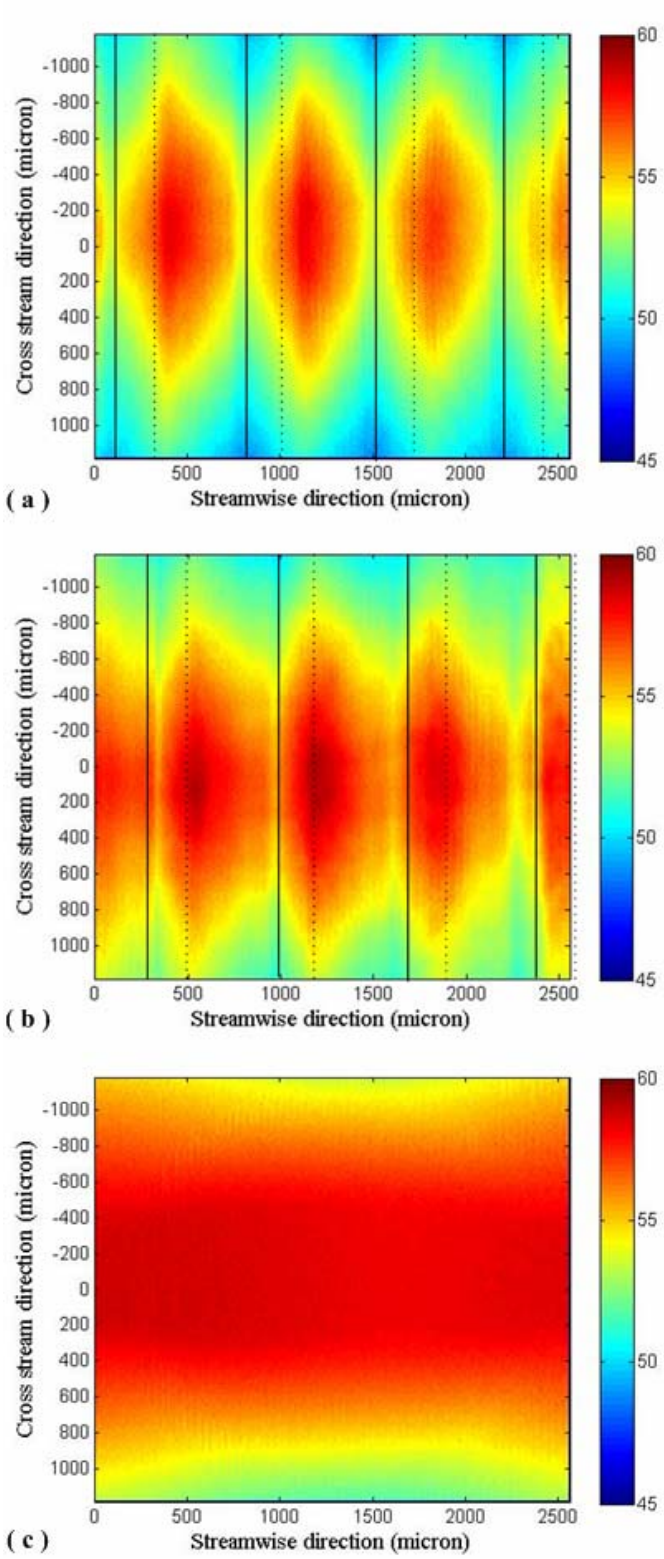

Figure 6.8 Contour maps of the oil-air interfacial temperature for three liquid thicknesses: (a) 0.5 mm (b) 1.0 mm (c) 2.7 mm for ΔT=37.5 ºC.

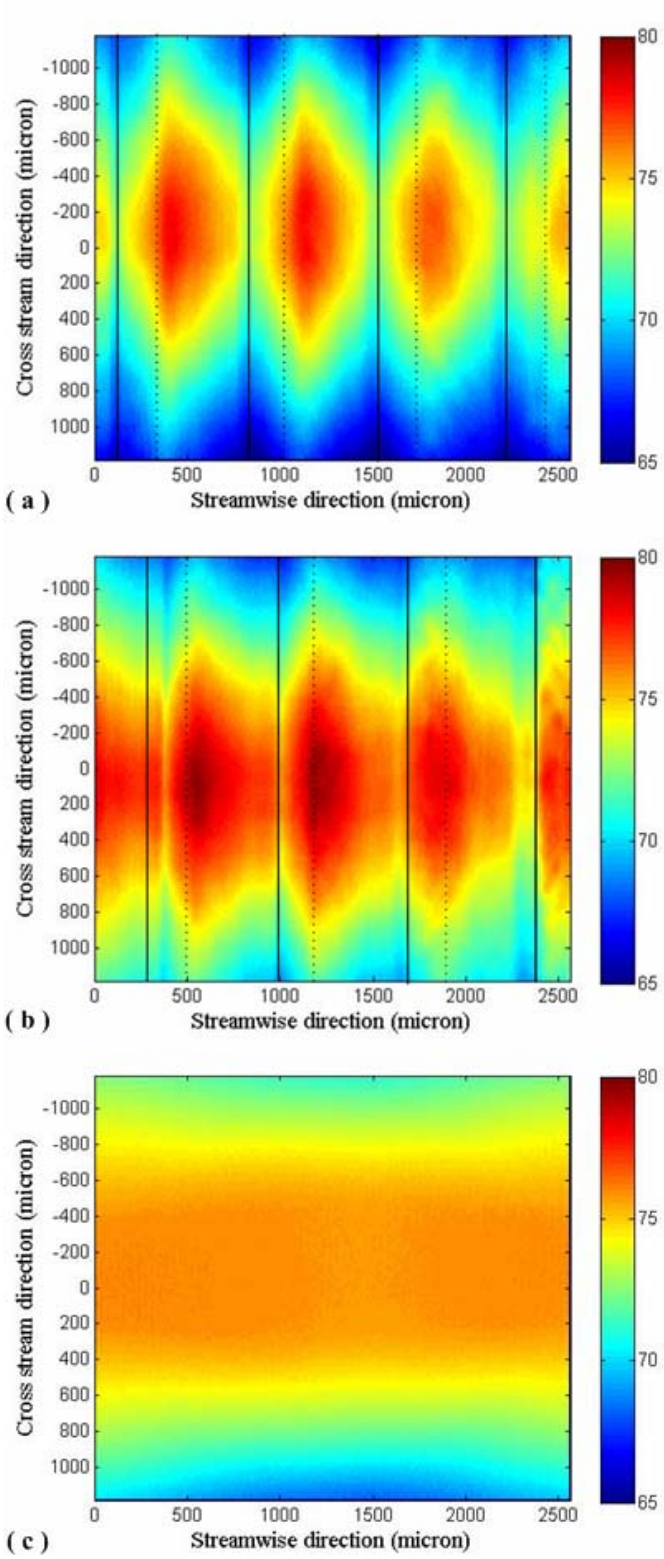

Figure 6.9 Contour maps of the oil-air interfacial temperature for three liquid thicknesses: (a) 0.5 mm (b) 1.0 mm (c) 2.7 mm for ΔT=57.5 ºC.

One notable trend in the axial temperature distribution for the 1.0 mm thickness is that the decrease in temperature is non-monotonic from the crest towards the 30-degree slope side of the ratchet. This trend can be more clearly observed in Fig.6.10, in which the streamwise profiles at the mid-section of the channel for 0.5 mm and 1 mm thicknesses are extracted from the contour plots of Figs 6.9 (a) and (b). For generating each profile, twenty pixels around the mid-section in the cross-stream direction are averaged. The non-monotonic trend for 1 mm thickness could be an indication of a more complex convection cell pattern at this thickness. However detailed flow field experiments are needed to confirm the exact differences in the convection patterns at different heights.

Recall that the interfacial velocity for 1 mm thickness was larger than that of 0.5 mm and 2.7 mm indicating an optimal liquid thickness for maximum velocity. Trends of interfacial velocity that were reported in Fig. 6.7 can be related to the interfacial temperature gradients seen in Fig. 6.10. The streamwise gradients of temperature, dT/dx, on either side of the peak temperature of the periodic thermal structures were obtained by curve fitting data along the slopes for three ratchet periods shown in Fig. 6.10 and for both liquid thicknesses. Table 6.1 indicates the temperature gradients corresponding to each ratchet period as well as the average gradient on each side of the ratchet. The interfacial temperature gradients can, in turn, be related to interfacial surface tension gradients through the temperature coefficient of surface tension, $d\sigma/dT$. Surface tension gradients are also presented in Table 3 based on $d\sigma/dT$ value from Table 4.1.

For a *net* interfacial velocity and hence thermally actuated pumping by surface tension forces, it is the *difference* between the interfacial surface tension on either side of the thermal structures that is of importance. It is clear from both Table 6.1 and Fig. 6.10 that for the 1 mm oil thickness, this difference in the temperature gradients between either side of the peak temperature of the thermal structure was much larger for 1 mm than for 0.5 mm. An estimate of the interfacial velocity by a simple force balance of viscous, inertia and surface tension forces is being pursued currently.

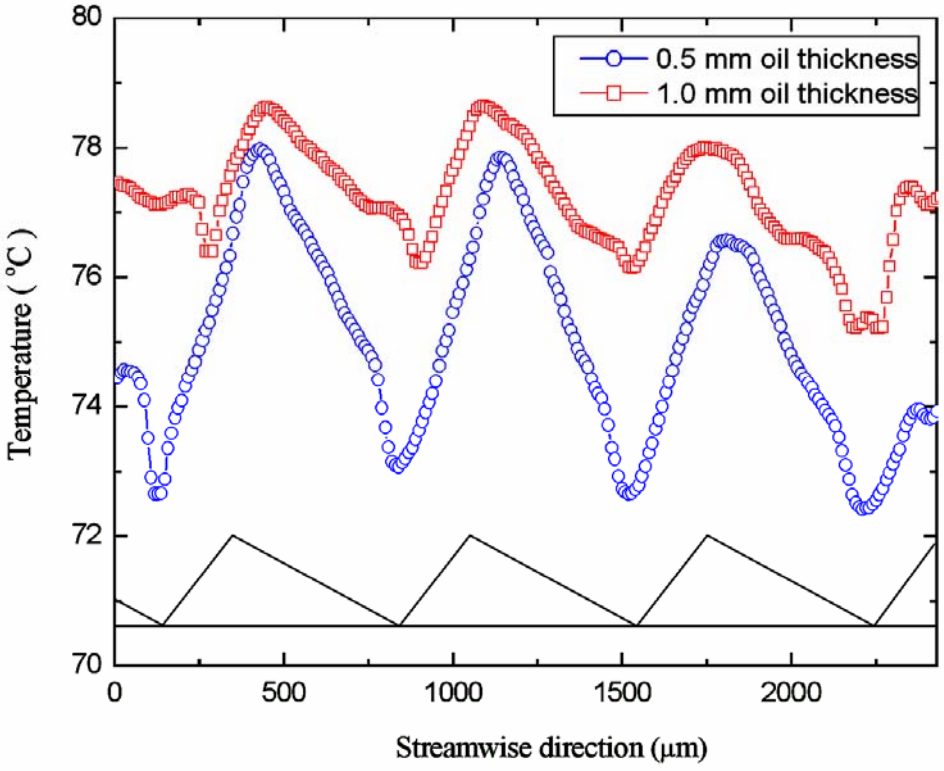

Figure 6.10 Streamwise gradients of temperature for two oil heights.

Table 6.1 Interfacial streamwise gradients of temperature and surface tension at the mid-channel plane.

	0.5 mm oil thickness						1.0 mm oil thickness					
	(1)	(2)	(3)	(4)	(5)	(6)	(1)	(2)	(3)	(4)	(5)	(6)
$\frac{dT}{dx}$ ($\times 10^{-2}$ °C/μm)	1.75	1.78	1.54	1.16	1.43	1.11	1.41	1.48	1.03	0.48	0.62	0.58
$\left.\frac{dT}{dx}\right\|_{av}$ ($\times 10^{-2}$ °C/μm)	1.69			1.23			1.31			0.56		
$\frac{d\sigma}{dx}$ (N/m^2)	1.15			0.84			0.89			0.38		
$\left.\frac{d\sigma}{dx}\right\|_{net}$ (N/m^2)	0.31						0.51					

7 CONCLUSIONS AND RECOMENDATIONS

An experimental study of thermally actuated pumping caused by asymmetric streamwise surface tension gradients was presented. Streamwise variation in the force was caused by a vertical temperature difference across the liquid while asymmetry in this force was set up be use of repeated ratchet patterns on the surface. The Marangoni number was varied by two independent parameters-the surface-to-ambient temperature differential and the liquid-to-ratchet thickness.

Experimental measurements were made of liquid-air interface velocity through dye tracking, and of liquid-air interface temperature through infrared thermography for three liquid heights and two surface-to-ambient temperature differentials.

Results indicate that the interface velocity for the 1 mm liquid thickness was larger than that for the 0.5 mm and 2.7 mm thicknesses, suggesting an optimum height for peak net fluid velocity. Interfacial temperature maps for the 1 mm thickness layer indicate larger areas of high temperature for the 1 mm thickness, suggesting that there exists an optimum thickness for high heat transfer coefficient.

Streamwise interface temperature profiles indicate more disproportionate streamwise gradients on either side of the ratchet crest for 1 mm thickness compared with 0.5 mm and 2.7 mm thicknesses. Because streamwise temperature gradients are directly related to streamwise surface tension gradients, the net asymmetry in surface tension force is larger for the 1 mm thickness.

Since there are many kinds of multi-layer liquid phenomena in engineering and industry application such as film processes, multilayer extrusion, and multilayer

coating, the problem of convection in two immiscible liquid layers has been of interest in recent years. The net flow induced by thermally actuated pumping in two immiscible liquid layers could also happen through surface tension gradients at the interface between the liquid layers or buoyancy forces. So, the study in the two immiscible liquid layers is recommended. In addition to, it is recommended the study of the effect of ratchet geometry, liquid surface deformation due to convection, and application of surfactant in order to more understand the effectiveness of the asymmetric surface.

BIBLIOGRAPHY

[1] Mukherjee, S. and Mudawar, I., 2003, "Pumpless Loop for Narrow Channel and Micro-Channel Boiling," *Journal of Electronic Packaging*, Vol. 125, pp. 431-441.

[2] Maydanik, Y.F., Vershinin, S.V., Korukov, M.A., and Ochterbeck, J.M., 2005, "Miniature loop heat pipes - A promising means for coolingelectronics,"*IEEE Transactions on Components and Packaging Technologies*, Vol. 28, No. 2, pp. 290-296.

[3] Ivanova, M., Avenas, Y., Schaeffer, C., Dezord, J.B., and Schulz-Harder, J., 2006, "Heat pipe integrated in direct bonded copper (DBC) technology for cooling of power electronics packaging," *IEEE Transactions on Power Electronics*, Vol. 21, No. 6, pp. 1541-1547.

[4] Chen, P.C. and Lin, W.K., 2001, "Experimental study of capillary pumped loop," *Transactions of the Aeronautical and Astronautical Society of the Republic of China*, Vol. 33, No. 4, pp. 247-255.

[5] Meyer, L., Dasgupta, S., Shaddock, D., Tucker, J., Fillion, R., Bronecke, P., Yorinks, L., and Kraft, P., "A silicon-carbide micro-capillary pumped loop for cooling high power devices," *Proceeding of the 9th Annual IEEE Semiconductor Thermal Measurement and Management Symposium*, San Jose, CA, United States, March 11-13, 2003.

[6] Schatz, M. and Neitzel, G.P., 2001, "Experiments on thermocapillary instabilities," *Ann. Rev. Fluid Mech.*, Vol. 33, pp. 93-127.

[7] Koschmieder, E. L., "Benard Cells and Taylor Vortices," Cambridge university press, 1993.

[8] Cerisier, P. and Lebon, G., 1996, "Surface Deflection in Benard-Marangoni Convection," *Lecture Notes in Physics*, Vol. 467, pp. 117-133.

[9] Linke, H., Aleman, B. J., Melling, L. D., Taormina, M. J., Francis, M. J., Dow-Hygelund, C. C., Narayanan, V., Taylor, R. P., and Stout, A., 2006, "Self-Propelled Leidenfrost Droplets," *Physical Review Letters*, Vol. 96, pp. 154502_1-154502_4.

[10] Strook, A.D., Ismagilov, R.F., Stone, H.A., and Whitesides, G.M., 2003, "Fluidic Ratchet Based on Marangoni-Benard Convection," *Langmuir*, Vol. 19, pp. 4358-4362.

[11] Binghong, Z., Qiusheng, L., and Zemei, T., 2004, "Raleigh-Marangoni-Benard Instability in Two-layer Fluid System," *ACTA Mechanica Sinica*, Vol. 20, No.4, pp. 366-373.

[12] Kang, Q., Zhang, J.F., Hu, L., and Duan, L., 2003, "Experimental Study On Benard-Marangoni Convection by PIV and TCL," *Optical Technology and Image Processing for Fluids and Solids Diagnostics*, Vol. 5058, pp. 155-161.

[13] Johnson, D. and Narayanan, R., 1997, "Geometric effects on convective coupling and interfacial structures in bilayer convection," *Physical Review E*, Vol. 56, No. 5, pp. 5462-5472.

[14] Selamet, E., Arpaci, V.S., and Chai, A.T., 1994, "Thermocapillary-Driven Flow past the Marangoni Instability," *Numerical Heat Transfer*, Vol. 26, pp. 521-535.

[15] VanHook, S.J., Schatz, M.F., McCormick, W.D., Swift, J.B., and Swinney, H.L., 1995, "Long-wavelength instability in surface tension-driven Benard convection," *Physical Review Letters*, Vol. 75, No. 24, pp. 4397-4402.

[16] Ismagilov, R. F., Rosmarin, D., Gracias, D. H., Stroock, A. D., Whitesides, G. M., 2001, "Competition of Intrinsic and Topologically Imposed Patterns in Benard-Marangoni Convection," *Applied Physics Letters*, Vol. 79, No. 3, pp. 439-441.

[17] Koschmieder E. L. and Prahl, S. A., 1990, "Surface tension-driven Benard convection in small containers," *Journal of Fluid Mechanics*, Vol. 215, pp. 571-583.

[18] Alexeev, A., Gambaryan-Roisman, T., and Stephan, P., 2005, "Marangoni convection and heat transfer in thin liquid films on heated walls with topography: Experiments and numerical study," *Physics of Fluids*, Vol.17, 062106.

[19] Krebs, D., Narayanan, V., Liburdy, J. A., and Pence, D. V., 2008, " Local Wall Temperature Measurement in Microchannel Boiling Flows Using Infrared Thermography," HT2008-56253, *Proceedings of the 2008 Summer Heat Transfer Conference*, Jacksonville, Florida, August 10-14, 2008.

APPENDICES

APPENDIX A: PRELIMINARY EXPERIMENTS - OPEN LOOP SYSTEM

.

The specific objective of the preliminary experiments is to confirm experimentally thermally actuated pumping due to Rayleigh-Benard convection an asymmetric topology. In order to quantify thermally actuated pumping, the global mass flow rate induced by pumping was measured as a function of surface-to-ambient temperature differential and liquid layer thickness in the open loop system.

A.1 Test Section

Figure A.1 shows a schematic of the test section of the open loop pump. It was composed of a housing that formed the sidewalls of the open channel, a surface with asymmetric structures (ratchets) that formed the bottom of the open channel, heating plates, and insulating plates. The major dimensions of the test section were 0.33 m x 0.178 m x 0.092 m. The ratcheted surface together with the housing formed the open channel. The housing was made of a thermally insulative material (polycarbonate) so that heat flowed into the channel predominantly from the bottom ratchet surface. The housing had only one inlet and exit ports. A viton o-ring, located along the interface between the housing and the ratchet plate, prevented leakage of liquid from the open channel. The bottom ratchet surface was formed of an aluminum plate with ratchets (triangular shape with 30°-60°-90° angles) machined into it using conventional milling. A schematic of the cross-sectional form of the ratchets with key dimensions is shown as an inset in Fig. A.1. The ratchets were 3.3 mm in height, and

7.6 mm in pitch; the relation between the pitch and the height was dictated by the angle of the ratchet. A sign (positive vs. negative) designating the direction of flow was assigned arbitrarily in relation to the steep and sloping faces of the ratchet as shown below in Fig. A.2 in order to identify the direction of pumping during experiments. In order to provide a temperature differential between the surface and the ambient air for thermally-induced convection, heating plates of aluminum-alloy were affixed to the base of the ratchet surface. Six 3.3 mm diameter cartridge heaters, located in a heating block below the ratchet plate, provided the necessary heat input. They were powered by a variac. Thermally conductive grease (OMEGATERM®201 Silicone paste) was applied between the heating plates and the ratcheted surface. The sides and bottom of the heating block were insulated using calcium silicate plates. Electrical power to the heaters was monitored by recording the current and voltage using multimeters. .Calibrated Chromel-Alumel (Type K) thermocouples were inserted at six axial locations and three vertical locations in the heating plate to determine the heat flux. The thermocouples closest to the ratchet plate were located 5mm below the ratchet plate and were used to estimate the ratchet surface temperature. Thermocouple data were obtained through data acquisition system (SCXI-1001, National Instruments) using a LabVIEW® program. This SCXI-1001 system has multi-channels and includes built-in cold junction compensation.

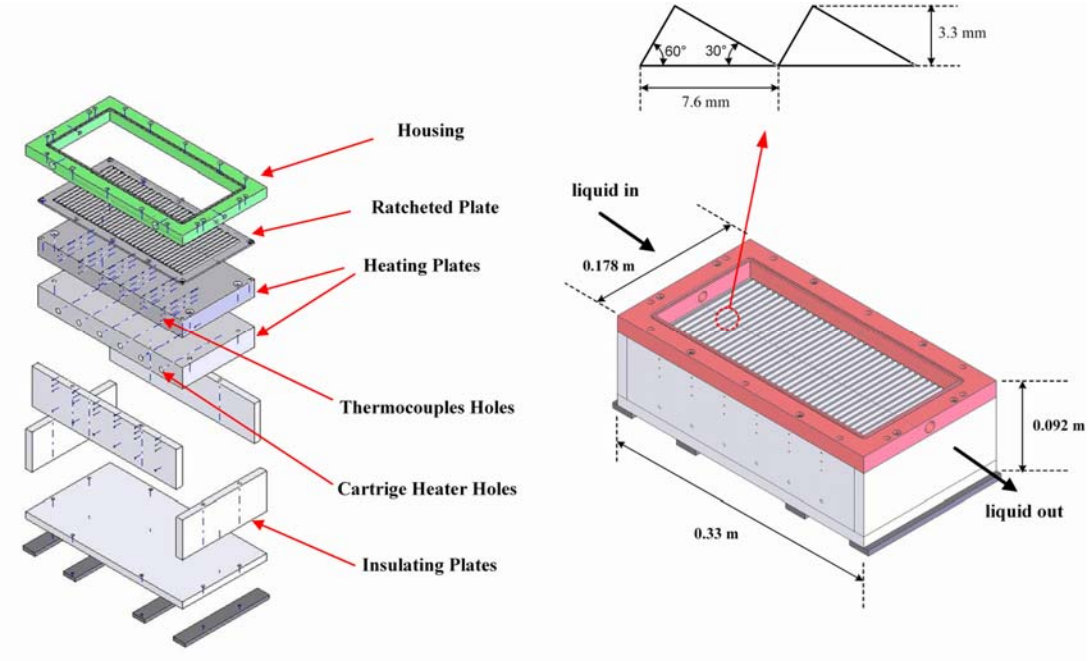

Figure A.1 Schematic of the test section for the open loop system.

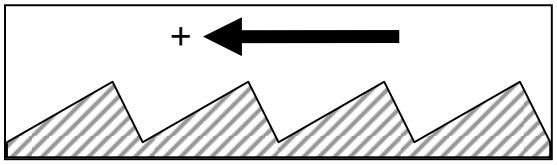

Figure A.2 Cross section of ratchet designating the positive direction of fluid travel.

A.2 Experimental Set-up

Figure A.3 shows a schematic of the experimental facility for the open loop experiments. It consisted of a computer controlled syringe pump (V6 Syringe Dispenser Module, KLOEHN Ltd.), inlet and outlet reservoirs, the test section, and a mass balance. The test section and outlet reservoir were placed on a sturdy steel platform with four leveling screws. The inlet reservoir was located on a separate vertical leveling platform (a vertical jack) that permitted independent movement of this reservoir for leveling of the reservoirs and the test section. Detailed explanation of the leveling method is presented in the following section on experimental procedure. A continuous fluid input was supplied to the inlet reservoir by syringe pump. In conjunction with an overflow port, this continuous fluid injection ensured that a constant fluid level was maintained in the inlet reservoir throughout the experiment. Such a configuration eliminated the contribution of hydrostatic pressure difference between the inlet and exit reservoirs causing pumping during the course of the experiment; hence the determined mass flow rate was only due to thermally-actuated pumping. The mass flow rate was determined using a catch-and-weigh method using a high accuracy mass balance (0.0001g resolution) and stopwatch (0.001 s resolution).

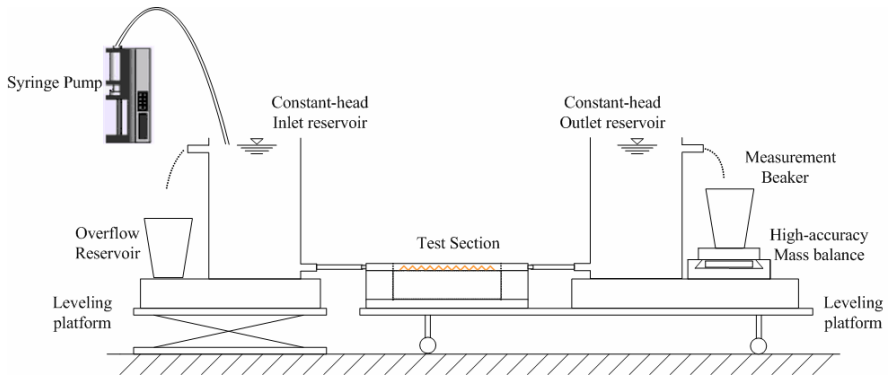

Figure A.3 Schematic of the experimental set-up for the open loop experiments.

A.3 Experimental Procedure

Table A.1 shows the experimental matrix for the open loop thermally actuated pumping. Two liquid heights, both corresponding to a buoyancy dominated driving force were studied. Note that the height of the ratchets being 3.3 mm did not permit a large Ma/Ra ratio. Three surface-to-ambient differential temperatures of 40, 60, and 80ºC were studied. Before starting an experiment, the ratchet plate was cleaned with a fine polishing cream (Mass® Metal Polishing Cream), isopropyl alcohol and de-ionized water, in that order. Silicone oil was then supplied to inlet & outlet reservoirs and test section. The thickness of the oil in the channel was measured with digital vernier caliper to a resolution of 0.01 mm. The height reported here is measured from the bottom of the ratchet surface. The most critical procedure in the open loop experiments was to ensure that the height of silicone oil in the inlet and outlet reservoirs was identical. The height of the inlet reservoir was adjusted using leveling platform until the overflow drip rate from the inlet reservoir overflow port matched that of the outlet reservoir. The overflow drip rate was measured with a stopwatch. The test facility was then left undisturbed until the dripping from the inlet and outlet reservoir overflows ceased (~1 hour).

Once no dripping through both reservoirs was ensured, the cartridge heaters were turned on. The surface temperature of ratchet plate was observed with thermocouples located 3 mm below the ratchet plate in heating block. When dripping of silicone oil from the outlet reservoir was observed, the silicone oil was supplied to the inlet reservoir using the syringe pump. This procedure allowed for a continuous fluid input into the inlet reservoir so as to maintain a constant fluid level in the inlet

reservoir. Once the surface temperature of the ratchet plate reached steady state at the desired temperature, the measurement beaker was placed under the outlet reservoir overflow tube and the stopwatch was started. After one hour, the mass of the silicone oil in the beaker was weighed using a high accuracy mass balance. Based on weighed mass and elapsed time, the mass flow rate by thermally-actuated pumping was determined. It should be noted that fluid was collected over a large time period to quantify the mass in order to increase the accuracy of the measurement as well as to reduce the uncertainty in time due to the coordination between the stop clock and placement of the beaker (~1 second). The near-surface thermocouple temperatures and the electrical power input data were recorded as well. The system was then turned off, the oil was removed from the system, and the test section was allowed to cool overnight.

The above experimental procedure allowed for quantifying pumping from the inlet to the exit reservoir alone, because of the overflow port of the inlet reservoir. During initial experiments, it was observed that fluid motion occurred in both directions; however the net bulk fluid motion occurred in only one direction. Hence, in order to try to determine the net pumping rate, it was necessary to reverse the orientation of the ratchets (see Fig. A.2) and redo each experiment. Thus, the next day, the ratchet plate was rotated 180 degrees, then the test section was assembled in the same manner as the day before and the testing was repeated.

Table A.1 Summary of test plan used for data collection in the open loop

Average ratchet surface temperature (ºC)	**Oil layer thickness (mm)**	**Ratio oil thickness to ratchet height**	***Ma***	***Ra***	***Ma/Ra***	**Dominant driving force (Buoyancy / Surface tension)**
60	5	1.52	153,015	513,265	0.3	Buoyancy
	14	4.24	428,443	11,267,195	0.04	Buoyancy
80	5	1.52	229,523	769,898	0.3	Buoyancy
	14	4.24	642,664	16,900,792	0.04	Buoyancy
100	5	1.52	306,031	1,026,530	0.3	Buoyancy
	14	4.24	856,887	22,534,390	0.04	Buoyancy

A.4 Data Reduction and Uncertainty Analysis

A.4.1 Data reduction-Mass flow rate

As noted in Chapter A.3, fluid flow occurs from the inlet to the exit reservoir for both positive and negative ratchet orientations. The net mass flow rate due to thermally actuated pumping was determined as the difference between the mass flow rates recorded between the two orientations of the ratchets. Mass flow rate for a particular ratchet orientation was determined by a catch-and-weigh method using a high accuracy mass balance (0.0001g resolution) and stopwatch (0.001 s resolution). The amount of silicone oil that flowed from the inlet to the exit reservoir and into the measurement beaker was determined for a one-hour interval. The recorded mass (m) was then divided by the measurement time interval (t) to determine the time averaged mass flow rate ($\dot{m}$),

$$\dot{m} = \frac{m}{t} \tag{A.1}$$

A.4.2 Uncertainty in Thickness of silicone oil

The thickness of the silicone oil in the channel was measured 5 times using digital vernier caliper micrometer (0.01 mm resolution). Uncertainty in thickness of silicone oil consisted of bias error associated with resolution of micrometer and precision error for measurement. Uncertainty value in thickness of silicone oil is reported in Table A.2.

Table A.2 Uncertainty in thickness of silicone oil in open loop system

Thickness of silicone oil	Bias error (mm)	Precision error (mm)	u_d (mm)	%
5 mm	0.01	0.02	0.02	0.44
14 mm	0.01	0.02	0.02	0.16

A.4.3 Uncertainty in Temperature and Heat Flux

Heat flux supplied by cartridge heaters was calculated based on the calibrated thermocouples readings and the known vertical distance between thermocouples.

$$q'' = k\frac{\Delta T}{\Delta x} \tag{A.2}$$

The thermal conductivity of the heating plate (Aluminum-Alloy 6061) is k = 166 W/m-K. Uncertainty in the heat flux was determined by applying the Kline-McClintock method. Uncertainty in the heat flux consisted of uncertainty in property of material, uncertainty in temperature measurement, and uncertainty in the vertical distance measurement between thermocouples. A typical uncertainty value in material property of ± 2 % for thermal conductivity of heating plate was applied. Uncertainty in temperature measurement consisted of bias error associated with the calibration of thermocouples and precision error due to fluctuation of temperature during the experiment. Uncertainty values in the heat flux for 60 °C, 80 °C and 100 °C case of ratchet surface temperature are reported in Table A.3.

Table A.3 Uncertainty in heat flux in open loop system

Average ratchet surface temperature	u_T (°C)	$u_{\Delta T}$ (°C)	$u_{\Delta x}$ (mm)	u_k (W/m-K)	$u_{heat\ flux}$ (W/m^2)	%
60 °C	0.04	0.06	0.02	3.32	54.65	11.26
80 °C	0.04	0.07	0.02	3.32	99.98	13.07
100 °C	0.04	0.07	0.02	3.32	103.8	9.5

A.4.4 Uncertainty in Mass flow rate

The recorded mass of oil that flowed into the measurement beaker was divided by the measurement time interval to determine the time averaged mass flow rate (see Eq. A.1). Uncertainty in mass flow rate was determined by applying the Kline-McClintock method to Eq.A.1. Propagate error also was calculated for uncertainty in net mass flow rate. Appendix D shows details of how this uncertainty was determined. Uncertainty values in mass flow rate and net mass flow rate for three temperature differences reported in Table A.4.

Table A.4 Uncertainty in (net) mass flow rate in open loop system

	Mass flow rate				Net mass flow rate	
Temperature difference (°C)	5 mm positive (mg/min)	5 mm negative (mg/min)	14 mm positive (mg/min)	14 mm negative (mg/min)	5 mm (mg/min)	14 mm (mg/min)
40	16.7 (15.7 %)	16.7 (21.8 %)	16.7 (11.6 %)	16.7 (13.9 %)	23.6 (79.4 %)	23.6 (99.9 %)
60	16.7 (11.2 %)	16.7 (14.1 %)	16.7 (10.8 %)	16.7 (12.1 %)	23.6 (77 %)	23.6 (139.5 %)
80	16.7 (13.0 %)	16.7 (14.8 %)	16.7 (11.8 %)	16.7 (13.5 %)	23.6 (144.6 %)	23.6 (137.8 %)

A.5 Results and Discussion

Figure A.4 shows the mass flow rate for two different thicknesses, 5mm and 14mm, of silicone oil as a function of the surface-to-ambient temperature difference in the open loop system. Also plotted is the variation of mass flow rate with applied heat flux to the ratchet surface. Average heat fluxes of 483.62 W/m^2, 769.02 W/m^2, and 1092.57 W/m^2, as determined by Eq. A.2, were applied to the test device for the respective nominal ratchet surface temperatures of 60 °C, 80 °C and 100 °C. The average air temperature of the room during experiment was 20.6 °C. In the present study, the ratios of the Marangoni number to the Rayleigh number in 5 mm thickness and 14 mm thickness are 0.298 and 0.038 respectively. Therefore, buoyancy forces were the dominant driving force for convection at both liquid heights. Note that the thermally-actuated pumping was observed for both ratchet orientations. However, the flow rate for the positive direction (see Fig. A.2) was larger than that of negative direction in the both liquid thicknesses, indicating that the net flow direction was positive. Note that mass flow rate in either ratchet orientation did not increase continuously with increasing the temperature difference for either liquid thickness. The magnitude of mass flow rate for ΔT of 79.4 °C was lower than the values for the ΔT of 59.4 °C for all cases. Within the range of temperature differentials studied, the mass flow rate has a maximum at a ΔT of 59.4 °C for both liquid heights and ratchet orientations. The reason for this maximum is unclear since the buoyancy force increases with increase in surface-to-ambient temperature differential (see Table A.1). However, this trend is consistent between both liquid thicknesses. Also note that this plot shows only the fluid flow rate in one ratchet orientation as opposed to the net flow

rate. With an increasing the temperature difference across oil layer from 39.4 °C to 79.4 °C, the difference of mass flow rate values between the positive and negative ratchet direction decreased by 45.12 % and 27.54 % for 5 mm and 14 mm cases, respectively. Given this trend, the net flow direction could likely change with ΔT larger than 79.4 °C from positive direction to negative direction in both thicknesses. However, experiments with larger surface temperatures could be not performed because of the lack of integrity of the housing material (polycarbonate) at higher operating temperatures

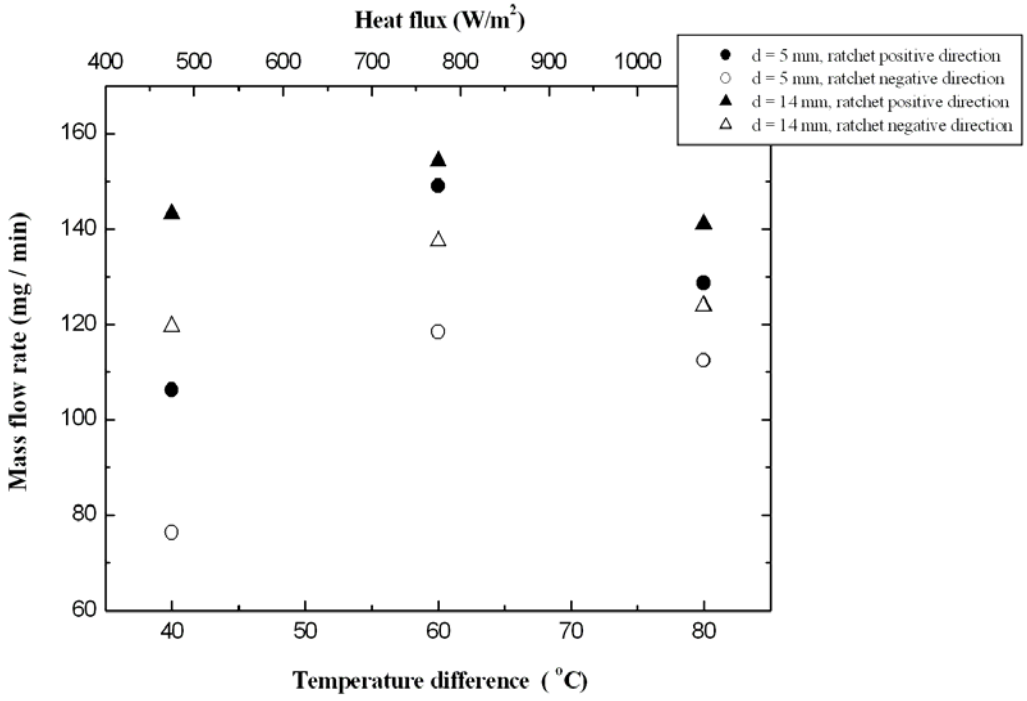

Figure A.4 Mass flow rate as a function of temperature difference and heat flux for open loop thermally actuated pumping

Figure A.5 shows the values of the determined net mass flow rates as a function of temperature difference and heat flux. Net mass flow rate was determined by subtracting mass flow rate with the negative ratchet orientation from the mass flow rate with the positive ratchet direction. For 5 mm oil thickness case, the net mass flow rate varied from 29.7 to 16.3 mg/min decreasing from 59.4 °C to 79.4 °C. In the 14 mm oil thickness experiments, the net mass flow rate varied from 23.6 to 17.1 mg/min with decreasing continuously with an increase in ΔT. The net mass flow rate of the 5 mm thickness oil layer was larger than that of the higher thickness layer of 14 mm at a temperature difference of 39.4 °C and 59.4 °C but was almost identical at a temperature difference of 80°C. It is seen that the ability of the thermally actuated pumping increases as the effect of buoyancy forces becomes small in the liquid. Thermally actuated pumping seems to also be inversely correlated with the Marangoni number for the range of the experiments studied. However, there is a positive correlation between the net mass flow rate and the ratio of Ma/Ra for ΔT = 39.4 °C and 59.4 °C.

The magnitudes of net mass flow rates in preliminary experiments are very small, and only slightly larger or even lower than the uncertainty in net mass flow rate. As noted in Chapter A.4, Uncertainty in net mass flow rate consisted of uncertainty in mass of oil based on both directions and uncertainty in elapsed time. The propagation error in net mass flow rate based on the mass measured of both direction cases is very large. For the lowest net mass flow rate of 17.1 mg, uncertainty was 23.6 mg. Hence it is difficult to comment with certainty on the net flow rate results. However, it can be stated with certainty that the net flow direction is positive. The low flow rate could

have largely to do with the single inlet and exit port in the channel side wall housing of the open loop test section (see Fig. A.1). This disadvantage was rectified in the closed loop test section of main experiments, which eliminates inlet and exit pressure losses present in the open loop test section. The open loop test section results emphasize the importance of proper design of inlet and exit ports for thermally actuated pumps.

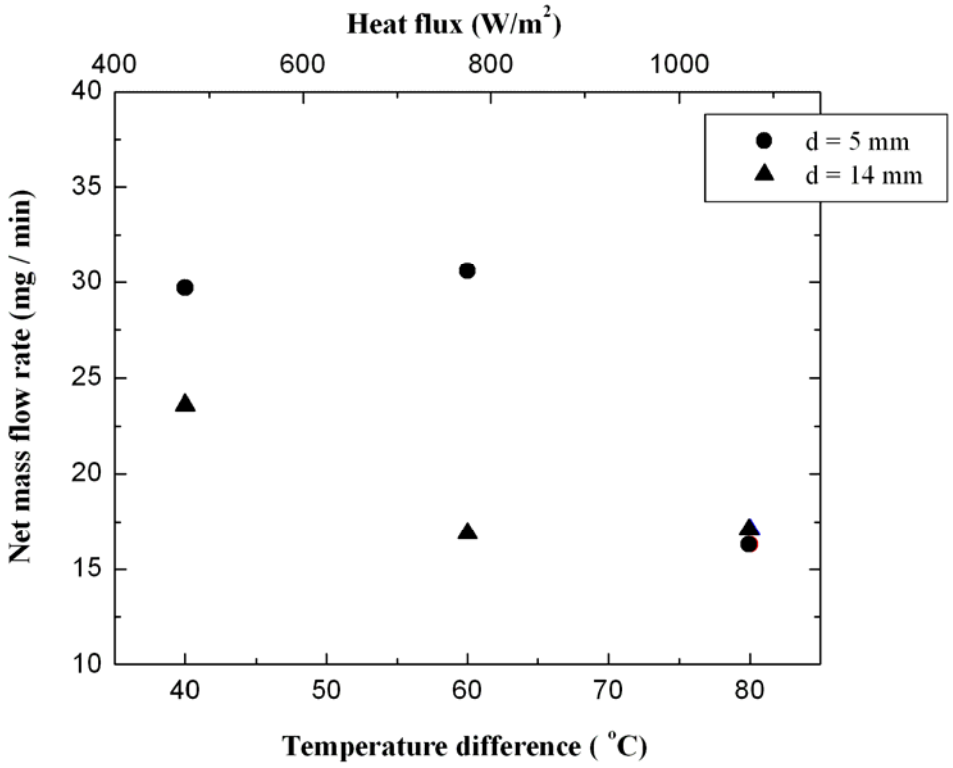

Figure A.5 Net mass flow rate as a function of temperature difference and heat flux for open loop pumping

APPENDIX B: STANDARD TEST PROCEDURES

B.1 Open Loop System

Assembling:

1. Clean the ratchet plate with a fine polishing cream, isopropanal alcohol and deionized water.
2. After painting the surface of the thermblock with thermally conductive grease (OMEGATHERM®201 silicone paste, OMEGA), bolt the ratchet plate to thermblock with 10 screws.
3. Viton O-ring is applied along the bottom side of the housing to prevent leakage.
4. Bolt the housing down with 8 bolts.
5. The reservoirs (1L) are connected to the housing with 2 tubes.
6. The insulating blocks are placed around the sides of the test section.

Leveling & Testing:

1. Whenever assemble the test model, check a level of each plate (thermblock, ratchet plate).
2. Supply silicon oil (SIL 180, Thermo Electron Corporation) to reservoirs and test model.
3. Adjust the height of the inlet reservoir until a drip rate from the inlet reservoir overflow tube matches that of the outlet reservoir overflow tube. A drip rate is measured by stopwatch.

4. Wait until the overflow dripping from the both reservoirs stop (about 1hour).
5. Measure the height of the fluid in the ratchet channel.
6. Turn on the variac which is connected in 6 cartridge heaters.
7. Initialize the both syringe pumps (refill-48000, speed-1000).
8. When start dripping overflow from the outlet reservoir, supply the oil to the inlet reservoir by the syringe pump 1 to allow for a continuous fluid input into the inlet reservoir so as to maintain a constant fluid level in the inlet reservoir.
9. Before the syringe pump 1 is empty, operate the syringe pump 2. Exchange repeatedly the both pumps during the testing.
10. After cleaning measurement beaker (80mL), put it on the digital scale (d=0.0001g). Then set ‘zero’ state.
11. Measure the surface temperature of ratchet plate with thermocouples (K-type).
12. When the surface temperature of ratchet plate reaches the steady state of the desired temperature, place the measurement beaker under the outlet reservoir overflow tube. Then start the digital stopwatch (0.001s resolution).
13. Record the surface temperature, voltage and ampere.
14. After 1hours pass, weigh the mass of the oil in the measurement beaker with digital scale (d=0.0001g).
15. Again after cleaning measurement beaker (80mL), put it on the digital scale. Then set ‘zero’ state.
16. Increase the input power to test other temperature cases

B.2 Closed Loop System

Assembling:

1. Clean the ratchet plate (360 brass) with a fine polishing cream, isopropanal alcohol and deionized water.
2. After painting the surface of the heating block with thermally conductive grease (OMEGATHERM®201 silicone paste, OMEGA), put the ratchet plate to heating block (1018 carbon steel).
3. Viton O-ring is applied along the bottom side of housing (PVC) to prevent leakage.
4. Bolt the housing down with 18 bolts.
5. The insulation wrap (AP/Armaflex) is applied around the sides of the test section.

Leveling, determining the oil thickness, and testing:

1. Whenever assemble the test model, check a level of each plate (heating block, ratchet plate, and housing) with small leveler.
2. Measure the weight of silicon oil (SIL 180, Thermo Electron Corporation) which will be added to the ratchet channel by the digital scale (0.0001g resolution).
3. Add the measured silicon oil to the ratchet channel.
4. Calculate the volume of the silicon oil from the measured weight by using the known density of silicon oil
5. Determine the thickness of added silicon oil from the calculated volume and

the dimensions of the ratchet channel.

6. Turn on the variac which is connected in 2 cartridge heaters.
7. Measure the heat flux from thermocouples (K-type) located at three axial location and three vertical locations in the heating block.
8. When the surface temperature of ratchet plate reaches the steady state of the desired temperature, take thermal transport images of the convection flow with IR camera.
9. Heat the dye (Oil Blue N) solution to the temperature of the ratchet plate.
10. Add a very small drop (~0.005mL) of dye solution in silicone oil to track the motion of the fluid.
11. Determine the net flow velocity with tracking of the motion of the dyed region using the image processing from CCD images.
12. Obtain the temperature distribution of the silicone oil layer from the IR images
13. Record the heat flux, voltage and current.

APPENDIX C: CALIBRATION

C.1 Calibration of thermocouples

The 18 thermocouples used in this study were calibrated using a constant temperature water bath and a hand held Omega® calibration unit with a NIST traceable RTD.

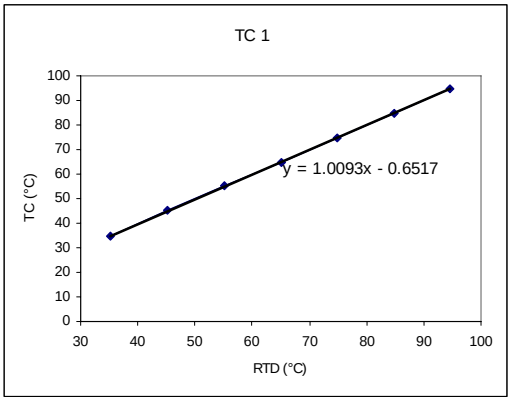

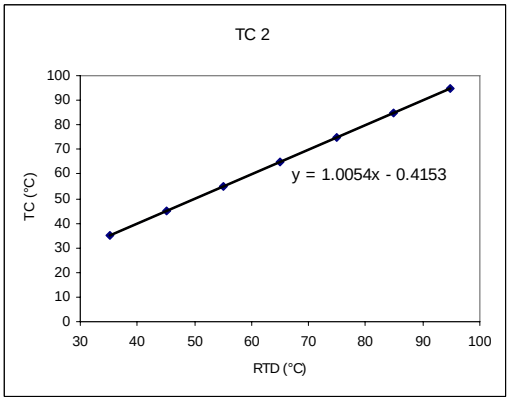

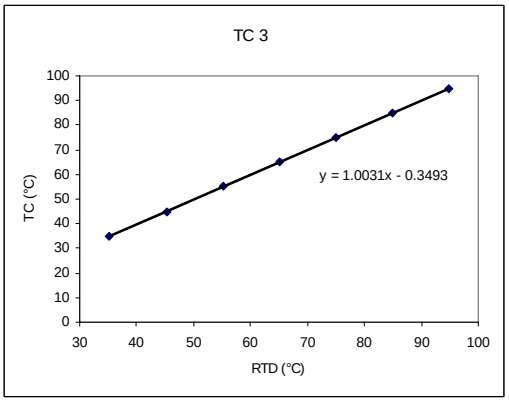

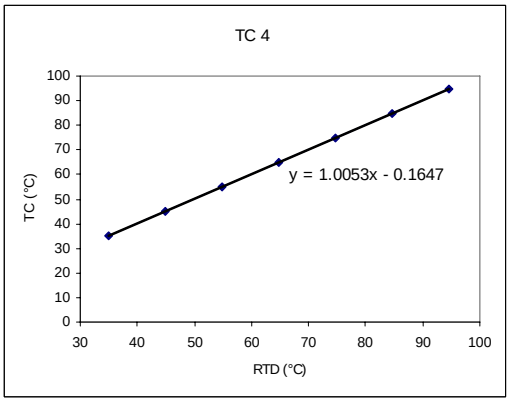

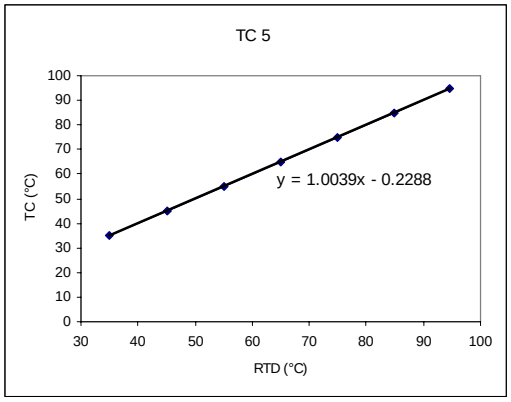
TC 5
y = 1.0039x - 0.2288
TC (°C)
RTD (°C)

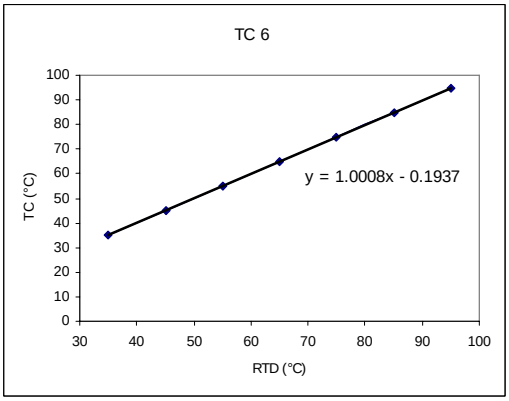
TC 6
y = 1.0008x - 0.1937
TC (°C)
RTD (°C)

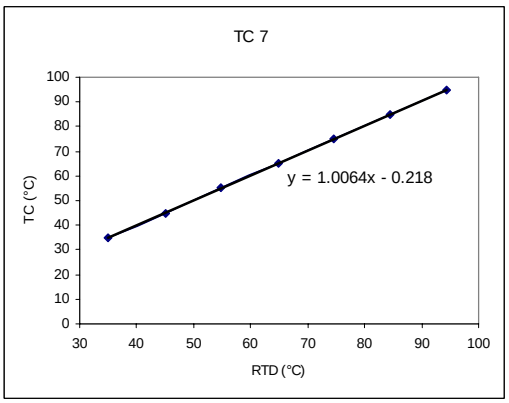
TC 7
y = 1.0064x - 0.218
TC (°C)
RTD (°C)

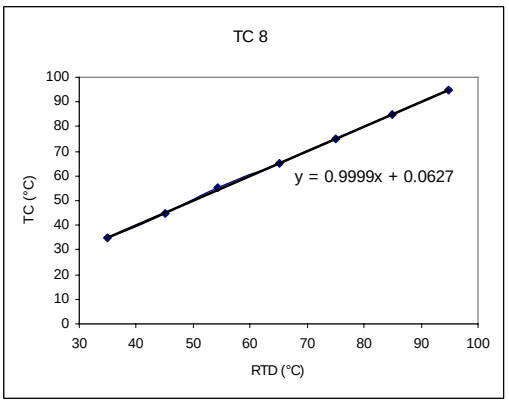
TC 8
y = 0.9999x + 0.0627
TC (°C)
RTD (°C)

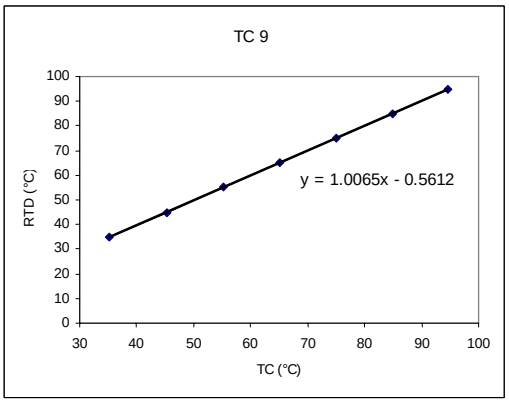
TC 9
y = 1.0065x - 0.5612
RTD (°C)
TC (°C)

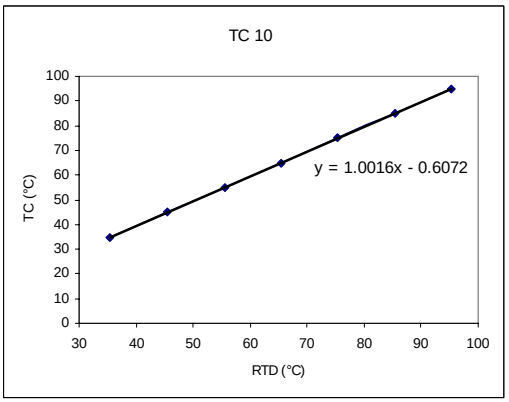
TC 10
y = 1.0016x - 0.6072
TC (°C)
RTD (°C)

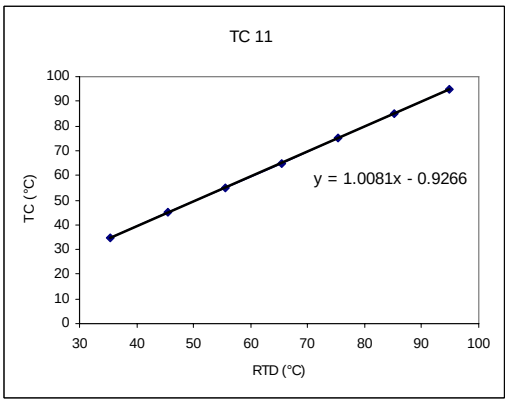
TC 11
y = 1.0081x - 0.9266
TC (°C)
RTD (°C)

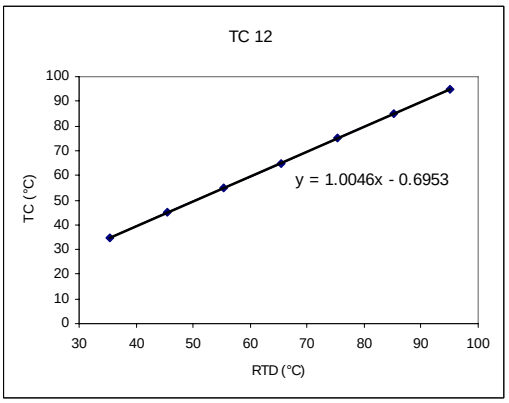
TC 12
y = 1.0046x - 0.6953
TC (°C)
RTD (°C)

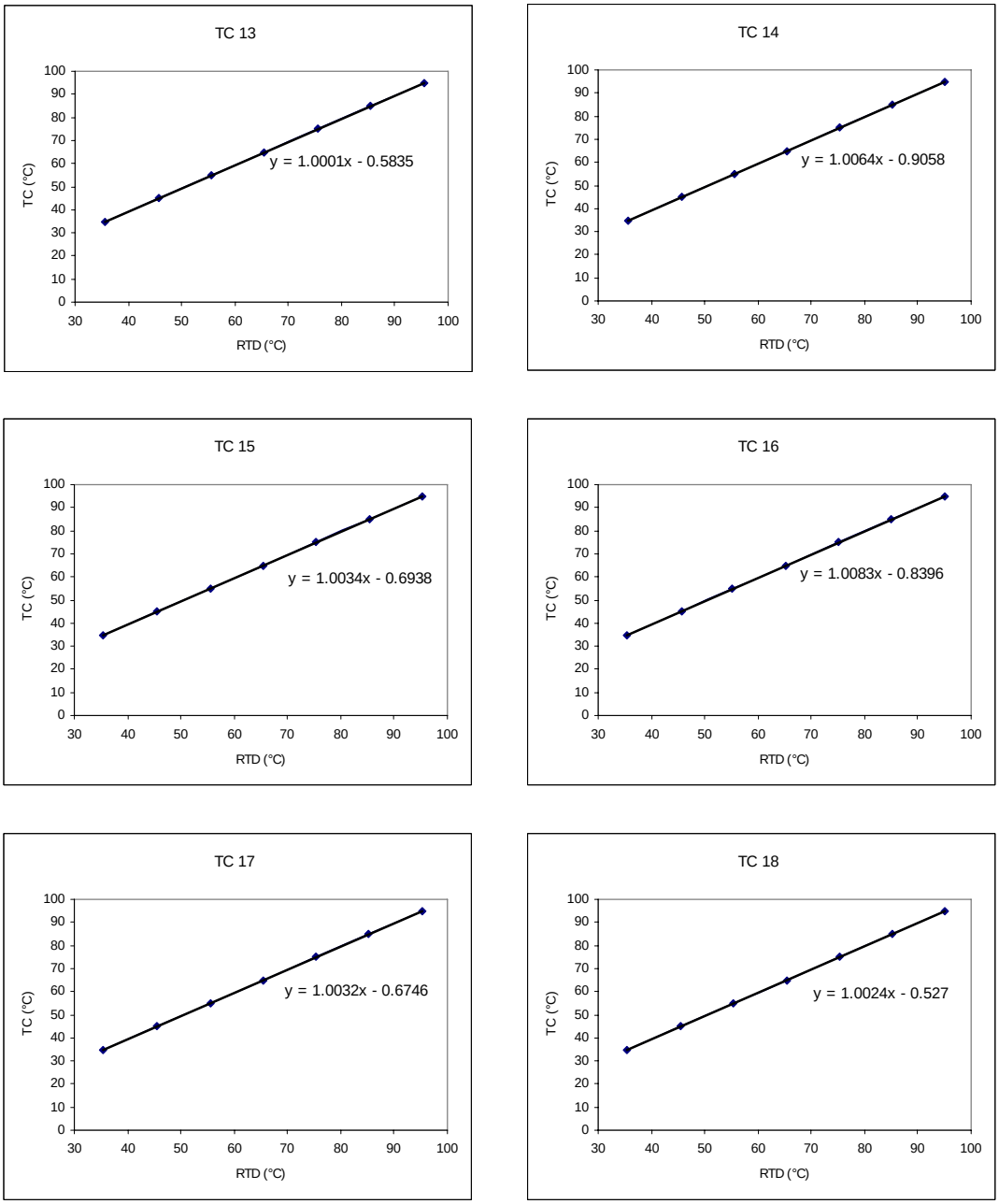

Figure C.1: Calibration curves for the thermocouples (TC)

APPENDIX D: UNCERTAINTY CALCULATIONS

D.1 Uncertainty in heat flux

Uncertainty in heat flux consisted of uncertainties in the temperature measurement, property value, and the distance between thermocouples measurement. Equation D.1 is the well known equation for heat flux, where ΔT is the vertical temperature difference between thermocouples, Δx is the vertical distance between thermocouples, and k is the thermal conductivity of the heating block.

$$q'' = k\frac{\Delta T}{\Delta x} \tag{D.1}$$

Uncertainty in heat flux was determined by applying the Kline-McClintock method to Eq. D.1 as shown below in Eq. D.2.

$$u_{q''} = \sqrt{\left(\frac{\partial q''}{\partial \Delta x}\cdot u_{\Delta x}\right)^2 + \left(\frac{\partial q''}{\partial k}\cdot u_k\right)^2 + \left(\frac{\partial q''}{\partial \Delta T}\cdot u_{\Delta T}\right)^2} \tag{D.2}$$

Uncertainty in temperature was obtained using the below equations.

$$u_T = \sqrt{(B_T)^2 + \left(\overline{S_T}\cdot t_{v,95\%}\right)^2} \tag{D.3}$$

$$B_T = \sqrt{(SE_{T,cal}\cdot t_{v,95\%})^2}, \qquad \overline{S_T} = \frac{S_T}{\sqrt{N}} \tag{D.4}$$

$$SE_{T,cal} = \left[\frac{\sum_{i=1}^{N}\{y_i - (ax_i + b)\}^2}{N-1}\right]^{1/2} \tag{D.5}$$

where, B_T is bias error associated with the calibration of thermocouples and $\overline{S_T}\cdot t_{v,95\%}$ is precision error. S_T is the standard deviation of data, N is total number of

data, and $t_{v,95\%}$ is t factor for a 95 % precision interval taken from the student-t distribution. In the bias error, $SE_{T,cal}$ is standard error of the curve fits for the thermocouples calibration. y_i is temperature of NIST traceable RTD and $ax_i + b$ is equation of calibration curve fit. Uncertainty in distance between thermocouples was also estimated using the above Eq. D.3. The estimated $u_{\Delta x}$ value was a constant for all cases and is equal to 0.0164 mm. The thermal conductivity of the heating block (1018 carbon steel) is k = 51.9 W/m·K. Since typical uncertainty in material property is ± 2%, uncertainty value in thermal conductivity of heating block is 1.038 W/m·K.

Table D.1 Uncertainty in heat flux for the average surface temperature of 60 °C

TC #	B_T (ºC)	$\overline{S_T} \cdot t_{v,95\%}$ (ºC)	u_T (ºC)	$u_{\Delta T}$ (ºC)	$u_{q''}$ (W/m^2)	%	TCs for heat flux
TC01	0.01297	0.02463	0.020438	0.028494	198.380	7.13	1_2
TC02	0.01203	0.02279	0.019855	0.027712	191.281	7.97	2_3
TC03	0.01119	0.02113	0.019332	0.028133	107.320	4.14	1_3
TC04	0.01128	0.02131	0.019389	0.027512	200.580	5.02	4_5
TC05	0.01149	0.02172	0.019518	0.027458	189.594	7.93	5_6
TC06	0.01116	0.02107	0.019313	0.027367	111.559	3.49	4_6
TC07	0.01114	0.02103	0.019298	0.027679	196.543	5.92	7_8
TC08	0.01201	0.02274	0.019842	0.028309	196.822	7.24	8_9
TC09	0.01258	0.02385	0.020192	0.027931	111.136	3.68	7_9
TC10	0.01198	0.02267	0.019819	0.028686	194.085	12.63	10_11
TC11	0.01346	0.02558	0.020739	0.028703	199.074	7.46	11_12
TC12	0.01202	0.02275	0.019843	0.028046	102.671	4.89	10_12
TC13	0.01182	0.02238	0.019725	0.028061	188.694	17.43	13_14
TC14	0.01220	0.02311	0.019959	0.028218	203.354	5.35	14_15
TC15	0.01218	0.02308	0.019948	0.028054	105.653	4.33	13_15
TC16	0.01212	0.02296	0.019910	0.028188	194.779	7.85	16_17
TC17	0.01219	0.02310	0.019953	0.028481	195.969	8.37	17_18
TC18	0.01279	0.02427	0.020323	0.028450	106.567	4.42	16_18

Table D.2 Uncertainty in heat flux for the average surface temperature of 80 °C

TC #	B_T (ºC)	$\overline{S_T} \cdot t_{v,95\%}$ (ºC)	u_T (ºC)	$u_{\Delta T}$ (ºC)	$u_{q''}$ (W/m^2)	%	TCs for heat flux
TC01	0.01226	0.02323	0.019996	0.028312	207.735	4.86	1_2
TC02	0.01234	0.02338	0.020043	0.028560	207.533	5.10	2_3
TC03	0.01283	0.02434	0.020346	0.028527	126.705	3.04	1_3
TC04	0.01174	0.02221	0.019672	0.028040	219.521	3.85	4_5
TC05	0.01224	0.02319	0.019982	0.028163	204.070	5.19	5_6
TC06	0.01202	0.02276	0.019846	0.027944	134.205	2.79	4_6
TC07	0.01244	0.02358	0.020104	0.028377	221.409	3.89	7_8
TC08	0.01231	0.02333	0.020026	0.028480	200.026	6.50	8_9
TC09	0.01267	0.02404	0.020250	0.028535	129.576	2.96	7_9
TC10	0.01225	0.02320	0.019987	0.028494	193.850	10.59	10_11
TC11	0.01277	0.02422	0.020309	0.028389	210.239	4.65	11_12
TC12	0.01200	0.02273	0.019837	0.028160	113.496	3.58	10_12
TC13	0.01237	0.02344	0.020063	0.028098	190.088	12.67	13_14
TC14	0.01174	0.02221	0.019672	0.027971	217.507	3.93	14_15
TC15	0.01208	0.02288	0.019885	0.028248	117.759	3.35	13_15
TC16	0.01182	0.02236	0.019720	0.028072	210.532	4.42	16_17
TC17	0.01223	0.02318	0.019979	0.028334	200.362	6.12	17_18
TC18	0.01242	0.02354	0.020092	0.028153	123.739	3.08	16_18

D.2 Uncertainty in flow velocity

Uncertainty in net flow velocity consisted of uncertainty in displacement measurement and the elapsed time measurement. Equation D.6 is the well known equation for a velocity, where Δx is the displacement of dyed region measured using the image processing and Δt is the elapsed time.

$$V = \frac{\Delta x}{\Delta t} \tag{D.6}$$

Uncertainty in net flow velocity was determined by applying the Kline-McClintock method to Eq. D.6 as shown below in Eq. D.7.

$$u_V = \sqrt{\left(\frac{\partial V}{\partial \Delta x} \cdot u_{\Delta x}\right)^2 + \left(\frac{\partial V}{\partial \Delta t} \cdot u_{\Delta t}\right)^2} \tag{D.7}$$

Uncertainty in displacement was largely dependent upon uncertainty in the image processing. Three uncertainty parameters were included in the image processing, that is, uncertainty in subtraction, binary converting, and median filtering. Uncertainty in the image processing was obtained by applying the sequential perturbation method. Uncertainty in the elapsed time was given by the manufacture of CCD camera to be 33×10-9 seconds.

Table D.3 Uncertainty in the net flow velocity

	0.5mm 60 °C	0.5mm 80 °C	1mm 60 °C	1mm 80 °C	2.7mm 60 °C	2.7mm 80 °C
$u_{subtraction}$ (mm)	0.251	0.044	0.237	0.194	0.164	0.156
u_{binary} (mm)	0.311	0.074	0.255	0.290	0.1670	0.320
$u_{filtering}$ (mm)	0.298	0.369	0.368	0.345	0.302	0.135
$u_{\Delta x}$ (mm)	0.499	0.379	0.507	0.491	0.382	0.381
$u_{\Delta t}$ (min)	5.5E-10	5.5E-10	5.5E-10	5.5E-10	5.5E-10	5.5E-10
u_V (mm/min)	0.0499	0.0379	0.0507	0.0491	0.0382	0.0381
%	14.39	8.06	9.56	5.68	10.96	5.38

D.3 Uncertainty in the depth of silicone oil

The depth of the silicone oil (d) was determined from the known density of oil (ρ), mass of added oil (m), and the area of the ratchet channel (A).

$$d = \frac{m}{\rho \cdot A} \tag{D.8}$$

Uncertainty in the depth of the silicone oil was determined by applying the Kline-McClintock method to Eq. D.8 as shown below in Eq. D.9.

$$u_d = \sqrt{\left(\frac{\partial d}{\partial m} \cdot u_m\right)^2 + \left(\frac{\partial d}{\partial A} \cdot u_A\right)^2 + \left(\frac{\partial d}{\partial \rho} \cdot u_\rho\right)^2} \tag{D.9}$$

Uncertainty value in density is 18.62 kg/m^3 by applying typical uncertainty ± 2% in property. Uncertainty in the mass of silicone oil consisted of bias error associated with resolution of mass balance and precision error for mass measurement as shown below in Eq. D.10.

$$u_m = \sqrt{(B_m)^2 + \left(\overline{S_m} \cdot t_{v,95\%}\right)^2}, \quad \overline{S_m} = S_m / \sqrt{N} \tag{D.10}$$

Uncertainty in the area of the ratchet channel was obtained by the following steps.

- Measured the weight of test section without silicon oil
- Measured the weight of test section added fully the silicon oil to the ratchet channel ➔ Calculated the mass of added fully the silicon oil
- Determined the area of the ratchet channel from the calculated the mass, the channel height, and the known density of silicon oil

$$A = \frac{m}{h \cdot \rho} \tag{D.11}$$

where, h is channel height, ρ is density of silicon oil, A is area of ratchet channel, and m is mass of added fully the silicon oil.

- Determined the uncertainty in the area of the ratchet channel by applying the Kline-McClintock method.

$$u_A = \sqrt{\left(\frac{\partial A}{\partial m}\cdot u_m\right)^2 + \left(\frac{\partial A}{\partial h}\cdot u_h\right)^2 + \left(\frac{\partial A}{\partial \rho}\cdot u_\rho\right)^2} \qquad \text{(D.12)}$$

Table D.4 The uncertainty in the depth of silicone oil for 1 mm thickness

m (g)	ρ (kg/m^3)	A (mm^2)	u_m (g)	u_ρ (kg/m^3)	u_A (mm^2)	u_d (mm)	%
2.262	931	1667	0.001	18.62	93.96	0.09	9.1

D.4 Uncertainty in interfacial temperature distribution

Uncertainty in interfacial temperature distribution obtained using IR system consisted of bias error associated with the calibration of the thermocouples used in calibration of the IRT images, precision error which is a standard deviation of temperature data obtained from IR images using calibration equation, and the calibration curve fit error of IR image. Uncertainty in temperature determined from IR images was obtained using the below equations.

$$u_T = \sqrt{(B_T)^2 + \left(\overline{S_{IR}} \cdot t_{v,95\%}\right)^2 + \left(SE_{IR,cal}\right)^2} \tag{D.13}$$

$$B_T = \sqrt{(SE_{tc,cal})^2 + (e_{T,STD})^2 + \left(\overline{S_{tc}} \cdot t_{v,95\%}\right)^2} \tag{D.14}$$

$$SE_{tc,cal} = \left[\frac{\sum_{i=1}^{N}\{y_i - (ax_i + b)\}^2}{N-1}\right]^{1/2}, \quad SE_{IR,cal} = \left[\frac{\sum_{i=1}^{N}\{y_i - (ax_i^3 + bx_i^2 + cx_i + d)\}^2}{N-1}\right]^{1/2} \tag{D.15}$$

where, B_T is bias error associated with the calibration of thermocouples, $\overline{S_{IR}} \cdot t_{v,95\%}$ is precision error based on a standard deviation of temperature data obtained from IR images and $SE_{IR,cal}$ is standard error of the curve fits for the IRT calibration. In the bias error, $SE_{tc,cal}$ is standard error of the curve fits for the thermocouples calibration, $e_{T,STD}$ is the error of the NIST traceable RTD used to calibrate thermocouples and $\overline{S_{tc}} \cdot t_{v,95\%}$ is precision error based on a standard deviation of temperature data obtained from thermocouples. *N* is total number of data, and $t_{v,95\%}$ is *t* factor for a 95 % precision interval taken from the student-*t* distribution.

Table D.5 Uncertainty in temperature obtained using IRT

Average ratchet surface temperature	Bias error (°C)	Precision error (°C)	Calibration curve fit error (°C)	u_T (°C)	%
60 °C	0.338	0.262	0.53	0.68	1.13
80 °C	0.338	0.199	0.53	0.66	0.83

D.5 Uncertainty in (net) mass flow rate in open loop system

Uncertainty in mass flow rate consisted of uncertainties in the mass of oil that flowed into the measurement beaker and in elapsed time measurement. Uncertainty in mass flow rate was determined by applying the Kline-McClintock method to Eq. A.1 as shown below in Eq. D.16

$$u_{\dot{m}} = \sqrt{\left(\frac{\partial \dot{m}}{\partial m}\cdot u_m\right)^2 + \left(\frac{\partial \dot{m}}{\partial t}\cdot u_t\right)^2} \tag{D.16}$$

Propagate error also was calculated for uncertainty in net mass flow rate as shown below in Eq. D.17

$$u_{\dot{m}_{net}} = \sqrt{\left(u_{\dot{m}_+}\right)^2 + \left(u_{\dot{m}_-}\right)^2} \tag{D.17}$$

Table D.6 The result data of mass flow rate test in open loop system

	Mass flow rate				Net mass flow rate	
Temperature difference (°C)	5 mm positive (mg/min)	5 mm negative (mg/min)	14 mm positive (mg/min)	14 mm negative (mg/min)	5 mm (mg/min)	14 mm (mg/min)
40	106.1	76.4	143.2	119.6	29.7	23.6
60	149.1	118.5	154.3	137.4	30.6	16.9
80	128.7	112.4	141.0	123.9	16.3	17.1

Table D.7 Uncertainty in (net) mass flow rate in open loop system

	Mass flow rate				Net mass flow rate	
Temperature difference (°C)	5 mm positive (mg/min)	5 mm negative (mg/min)	14 mm positive (mg/min)	14 mm negative (mg/min)	5 mm (mg/min)	14 mm (mg/min)
40	16.7 (15.7 %)	16.7 (21.8 %)	16.7 (11.6 %)	16.7 (13.9 %)	23.6 (79.4 %)	23.6 (99.9 %)
60	16.7 (11.2 %)	16.7 (14.1 %)	16.7 (10.8 %)	16.7 (12.1 %)	23.6 (77 %)	23.6 (139.5 %)
80	16.7 (13.0 %)	16.7 (14.8 %)	16.7 (11.8 %)	16.7 (13.5 %)	23.6 (144.6 %)	23.6 (137.8 %)

APPENDIX E: MATLAB® PROGRAM

```
%=========================================================================
% IMAGE PROCESSING TO ENHANCE RAW IMAGES
%=========================================================================

    clear;
    close all;
    clc;

% Reading reference image
    ref= imread('File0000.tif');

% Multiplying constant number (between 0 to 1)
% to reference image in order to reduce intensity
    ref=0.9*ref;

% Numbers of data
    nfiles=500;

% Reading data images
    for i=0:(nfiles-1)

        filename=strcat('File' , num2str(i,'%04d'),'.tif');
        data=imread(filename,'tif');

% Subtracting the pixel intensities between the data image and
% the reference image to remove the high intensity ratchet regions
        Subt = imsubtract(data,ref);

% 2D median filtering to reduce the surface noise
        Fil=medfilt2(Subt,[100 100]);

% Adjusting image intensity values
        Fil=imadjust(Fil);

% Binarizing the image
        Level=0;
        P=im2bw(Fil,Level);

% Writing final images
        imwrite(P,strcat('data', num2str(i,'%04d'),'.tif'));

    end
```

```
%=========================================================================
% TRACES BOUNDARY OF DYED REGION & DETERMINE CENTER OF MASS
%=========================================================================

    clear;
    close all;
    clc;

    BW=imread('data0000.tif');

    dim = size(~BW);
    col = round(dim(2)/2-10);
    row = min(find(~BW(:,col)));

    boundary = bwtraceboundary(~BW,[row, col],'N');
    imshow(BW)
    hold on;

    plot(boundary(:,2),boundary(:,1),'g','LineWidth',3);
    m=median(boundary);
    x=m(:,2)
    y=m(:,1)
    plot(x,y,'+r','MarkerSize',5)
    hold off
```

```
%=========================================================================
%MAIN PROGRAM FOR IR IMAGE CALIBRATION
%=========================================================================

clear all;
clc;

%Generate / load calibraion curve
%=========================================================================
disp('generate calibration curve');
[p,S,mu,order] = cal_curve_pixel();

%Calibration
%=========================================================================
disp('start calibration');

       filename_read = sprintf('0.5_60.lvm');

       disp(filename_read);

       %read in file
       %=================================================================
       [measured_val,rows,columns] = open_datafile(filename_read);
```

```
        %convert intensity to temp
        %================================================================
        for i = 1:rows
            for j = 1:columns
                for k = 1:(order+1)
                    poly(k)=p(i,j,k);
                end
                real_temp(i,j) = polyval(poly,measured_val(i,j),...
                            [],mu(i,j,:));
            end
        end

        %save file as *.lvm
        %================================================================
        dlmwrite('0.5_60_temp.lvm',real_temp)


function[measured_val,rows,columns] = open_datafile(filename)

%=========================================================================
% This function opens the *.lvm data files with the IR intensity
% values.
% Input: filename
% Output: matrix with the measured values (data), size of the matrix
%=========================================================================

        measured_val = dlmread(filename);
        [rows,columns] = size(measured_val);


function[coeff,str,u,order] = cal_curve_pixel()

%=========================================================================
% This function creates the calibration curve (coefficients of the
% curve fit) for each pixel.
% Input: none
% Output: 3D matrix with the coefficients for the fitting curve at
% each pixel
%=========================================================================

        files = 100;    %number of files for each Temperature level
        Temp_levels = [30,40,50,55,60,65,70,75,80]; %levels at which
        calibration was made
        Thermocouple_Temp =
        [30.04,40.19,49.10,55.39,59.63,64.91,70.05,74.53,80.09]; %refe
        rence temperature
        order = 2; % order of calibration curve fit equation

%open calibration files / create filename
%=========================================================================
for i = 1:length(Temp_levels)
    for j = 1:files

            filename = sprintf('%d_%d.lvm',Temp_levels(i),j);
```

```
        disp(filename);
        [measured_val,rows,columns] = open_datafile(filename);
        cal_matrix_same_level(:,:,j) = measured_val;   %data for one
        temp level
    end
        cal_matrix_same_level_sum = zeros(rows,columns);

    for k = 1:files
        cal_matrix_same_level_sum = cal_matrix_same_level_sum...
            +cal_matrix_same_level(:,:,k);
    end
    cal_matrix_same_level_average = cal_matrix_same_level_sum./files;
    cal_matrix(:,:,i) = cal_matrix_same_level_average;
 end

%=========================================================================
% cal_matrix is the matrix with all the averaged IR reference values
% at each pixel and at each temperature level (3D matrix)
%=========================================================================

%calculate coefficients for the polynomial fit
%=========================================================================
for i = 1:rows
    for j = 1:columns
        for k = 1:length(Temp_levels)
            x(k) = cal_matrix(i,j,k);
            y(k)=Thermocouple_Temp(k);
        end
        [p,S,mu] = polyfit(x,y,order);
        coeff(i,j,:) = p;
        str(i,j,:) = S;
        u(i,j,:) = mu;

    end

end
```

APPENDIX F: TEST SECTION PART DRAWINGS (CLOSED LOOP SYSTEM)

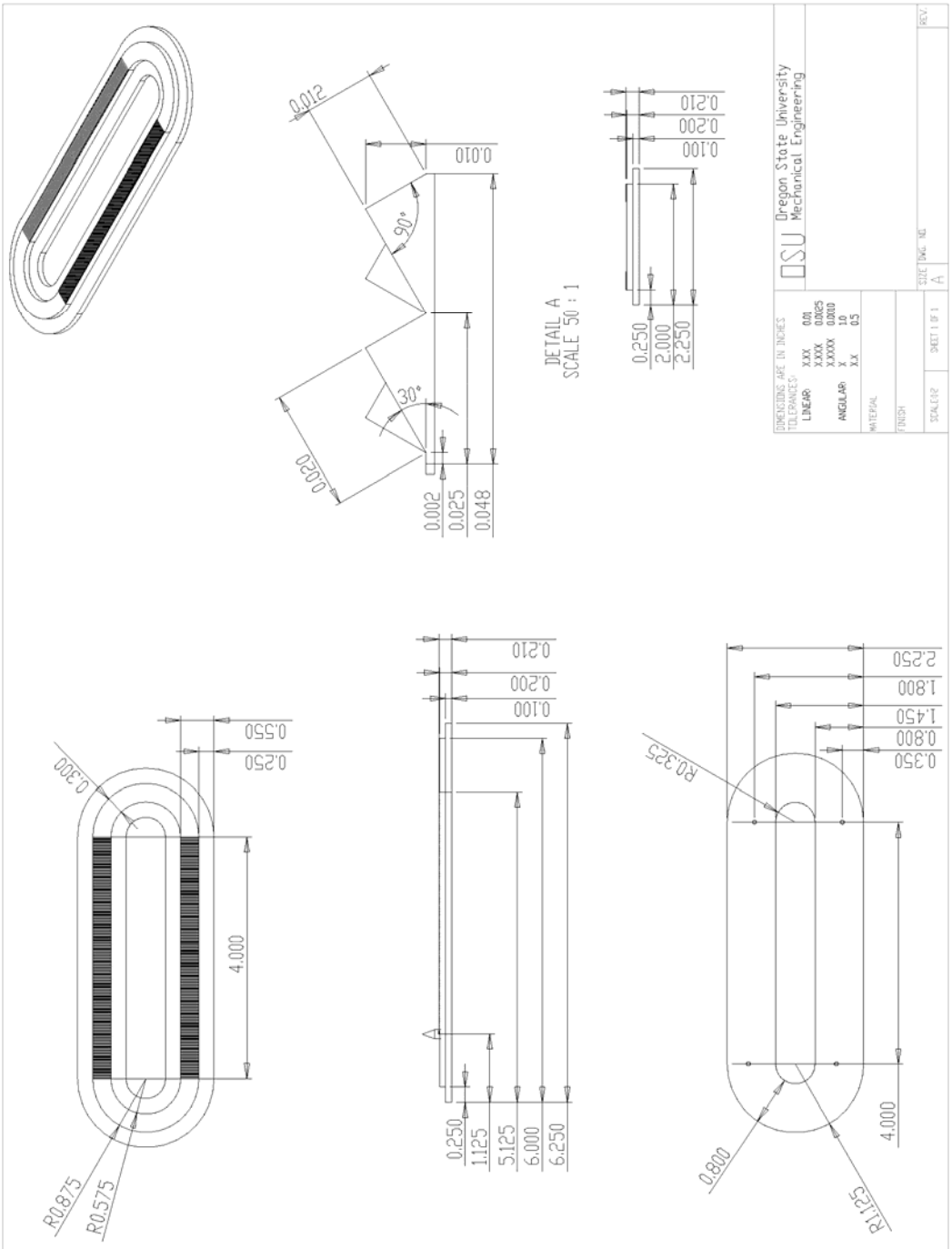

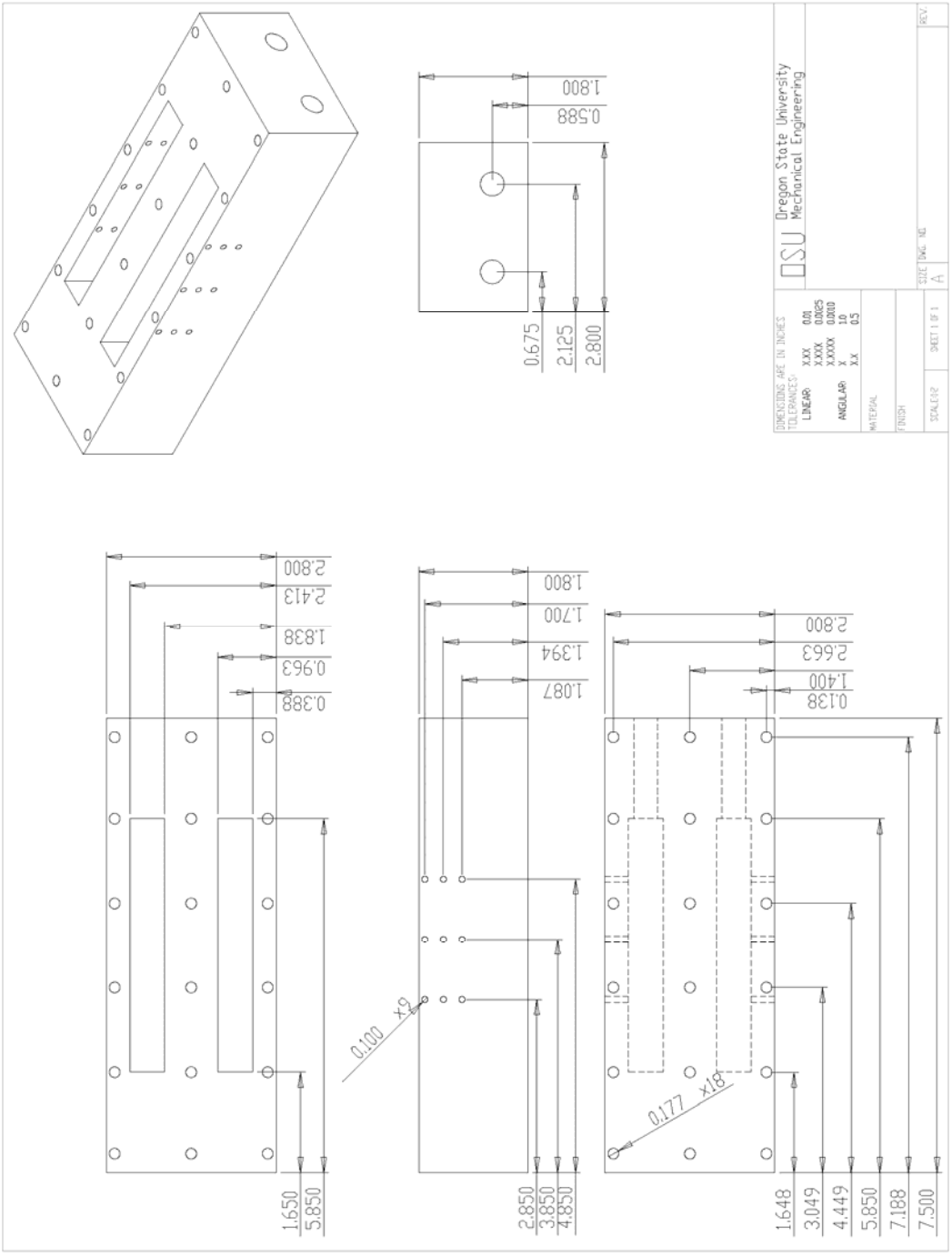
Oregon State University
Mechanical Engineering
OSU
DIMENSIONS ARE IN INCHES
TOLERANCES
LINEAR: XXX .01
XXXX .0025
XXXXX .0010
ANGULAR: X 1.0
X.X .5
MATERIAL
FINISH
SCALE:FIT
SHEET 1 OF 1
SIZE DWG. NO.
A
REV.
1.800
0.588
0.675
2.125
2.800
2.800
2.413
1.838
0.963
0.388
1.650
5.850
1.800
1.700
1.394
1.087
0.100 x9
2.850
3.850
4.850
2.800
2.663
1.400
0.138
0.177 x18
1.648
3.049
4.449
5.850
7.188
7.500

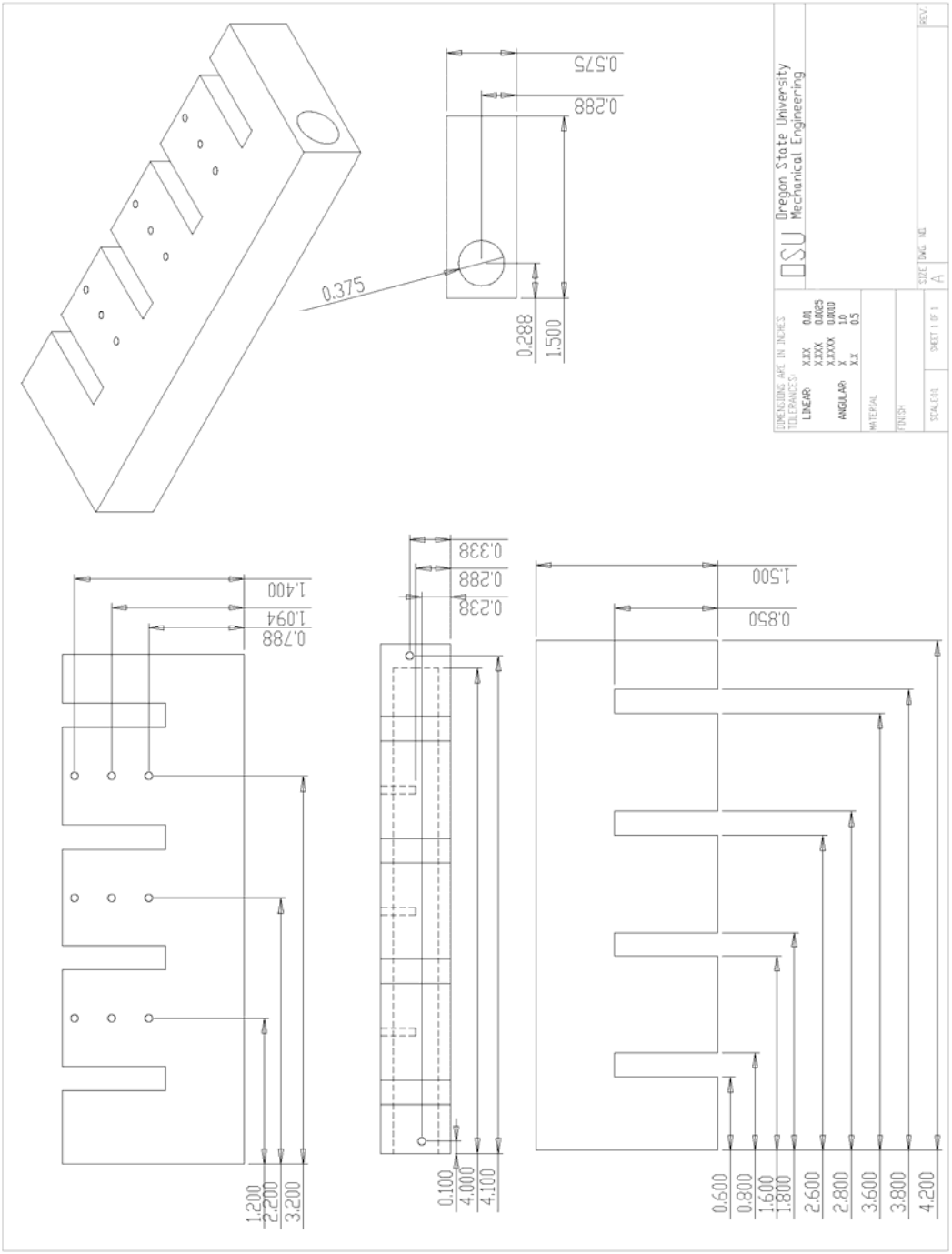
0.575
0.288
0.375
0.288
1.500
Oregon State University
Mechanical Engineering
DIMENSIONS ARE IN INCHES
TOLERANCES
LINEAR: XXX .01
XXXX .0025
XXXXX .0010
ANGULAR: X 1.0
X.X .5
MATERIAL
FINISH
SCALE:1/1
SHEET 1 OF 1
SIZE
A
DWG. NO.
REV.
1.400
1.094
0.788
1.200
2.200
3.200
0.338
0.288
0.238
0.100
4.000
4.100
1.500
0.850
0.600
0.800
1.600
1.800
2.600
2.800
3.600
3.800
4.200

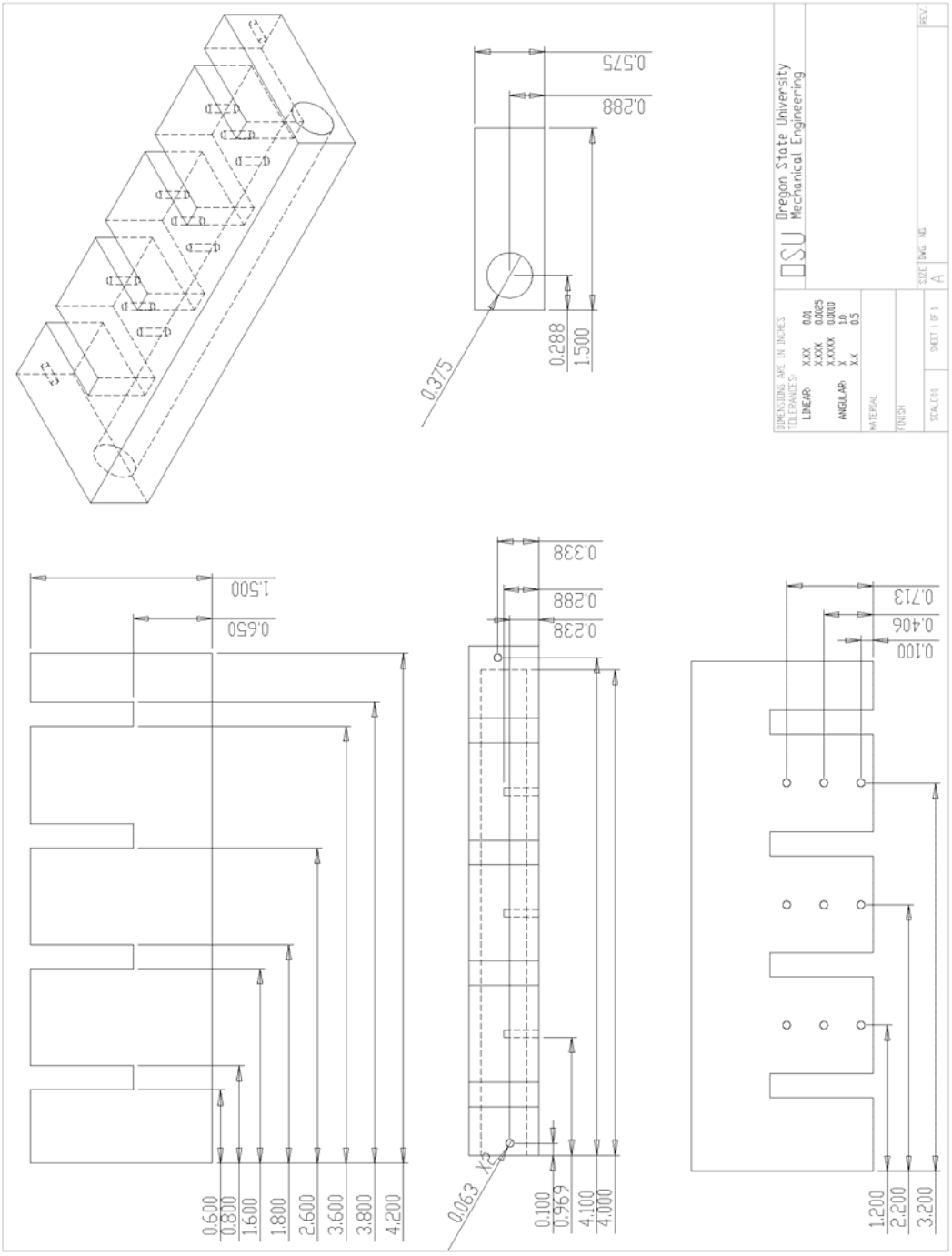
0.575
0.288
0.288
1.500
0.375
Oregon State University
Mechanical Engineering
DIMENSIONS ARE IN INCHES
TOLERANCES
LINEAR: XXX 0.01
XXXX 0.0025
XXXXX 0.0010
ANGULAR: X 1.0
X.X 0.5
MATERIAL
FINISH
SCALE:1/1
SHEET 1 OF 1
SIZE A
DWG. NO.
REV.
1.500
0.650
0.600
0.800
1.600
1.800
2.600
3.600
3.800
4.200
0.338
0.288
0.238
0.063 X 45°
0.100
0.969
4.100
4.000
0.713
0.406
0.100
1.200
2.200
3.200

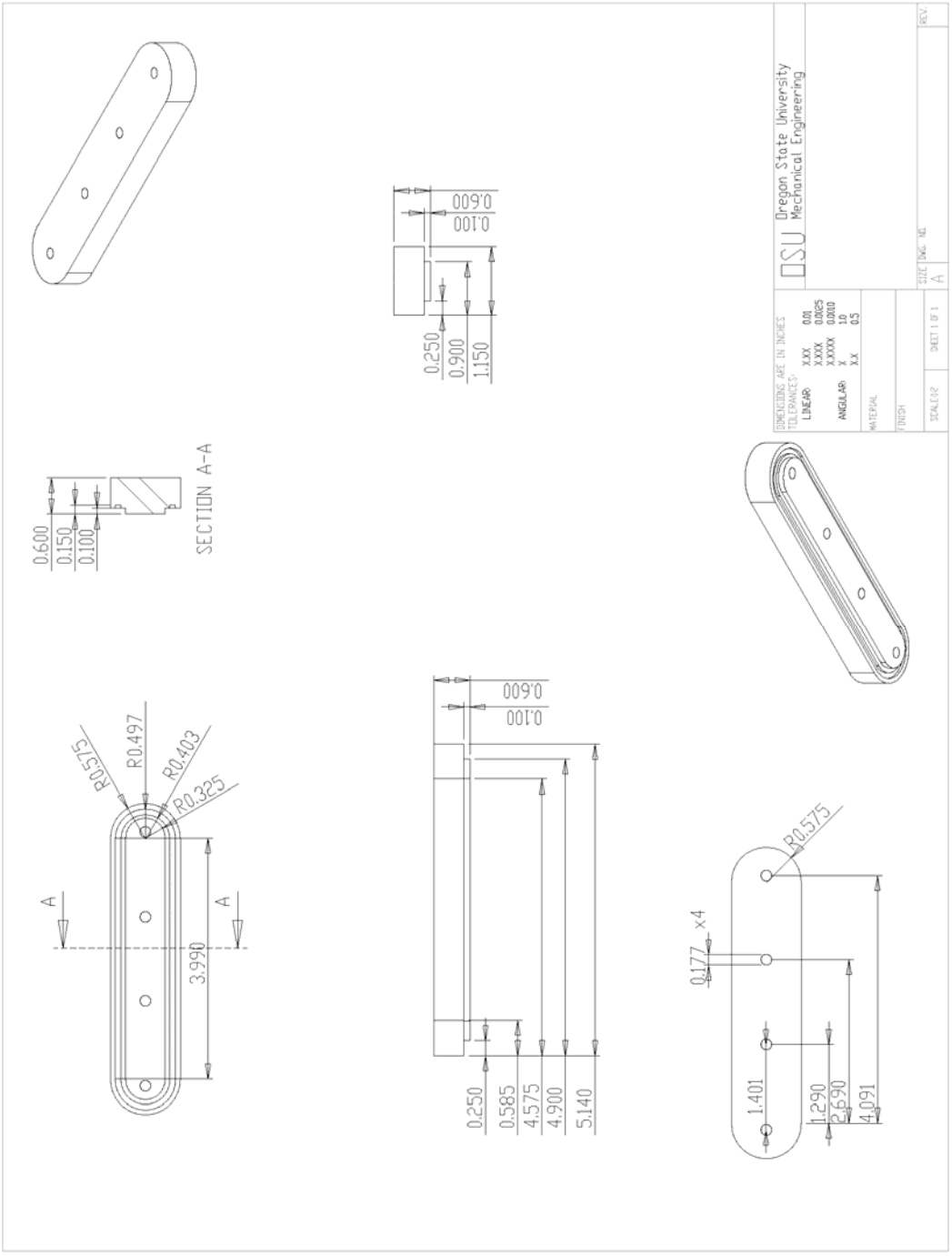
Oregon State University
Mechanical Engineering
OSU
DIMENSIONS ARE IN INCHES
TOLERANCES
LINEAR: XXX .01 XXXX .0025 XXXXX .0010
ANGULAR: X 1.0 X.X .5
MATERIAL
FINISH
SCALE:1/2
SHEET 1 OF 1
SIZE A
DWG. NO.
REV.
SECTION A-A
0.600
0.150
0.100
0.250
0.900
1.150
R0.575
R0.497
R0.403
R0.325
A
A
3.990
0.250
0.585
4.575
4.900
5.140
0.177 x4
1.401
1.290
2.690
4.091

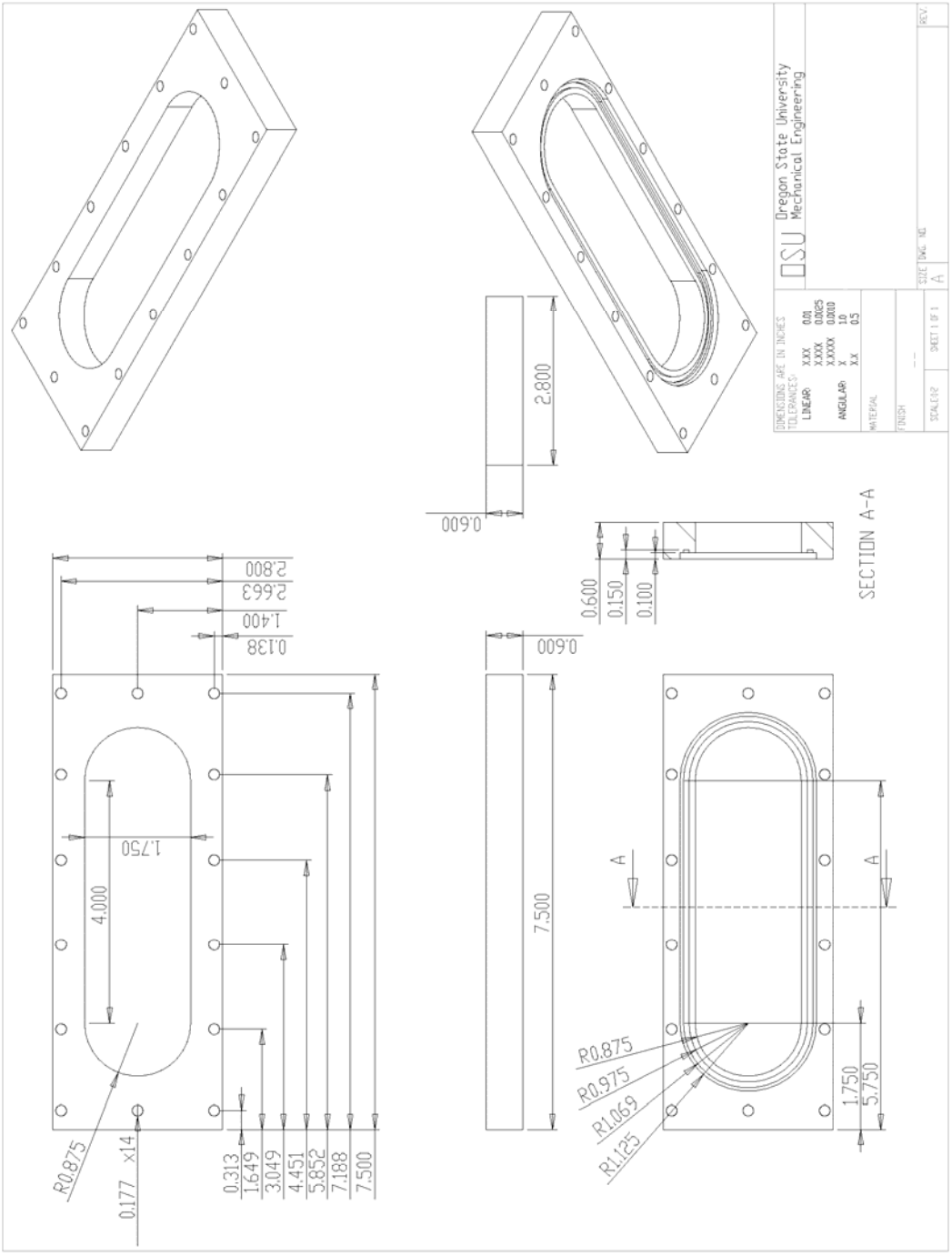
Oregon State University
Mechanical Engineering
OSU
DIMENSIONS ARE IN INCHES
TOLERANCES
LINEAR: XXX .001 XXXX .0025 XXXXX .0010
ANGULAR: X 1.0 X.X .5
MATERIAL
FINISH
SCALE:1/2
SIZE A
DWG. NO
REV
SHEET 1 OF 1
2.800
0.600
0.600
0.150
0.100
SECTION A-A
2.800
2.663
1.400
0.138
1.750
4.000
R0.875
0.177 x14
0.313
1.649
3.049
4.451
5.852
7.188
7.500
0.600
7.500
A
A
R0.875
R0.975
R1.069
R1.125
1.750
5.750